nature communications

Article

https://doi.org/10.1038/s41467-024-50881-1

Tumour-intrinsic endomembrane trafficking by ARF6 shapes an immunosuppressive microenvironment that drives melanomagenesis and response to checkpoint blockade therapy

Received: 4 January 2024

Accepted: 24 July 2024

Published online: 04 August 2024

Check for updates

Yinshen Wee[1,2,9,11], Junhua Wang[2,3,11], Emily C. Wilson[1,2], Coulson P. Rich[1,2], Aaron Rogers[1,2], Zongzhong Tong[1], Evelyn DeGroot[4], Y. N. Vashisht Gopal[4], Michael A. Davies[4], H. Atakan Ekiz[5], Joshua K. H. Tay[1,2], Chris Stubben[6], Kenneth M. Boucher[7], Juan M. Oviedo[1], Keke C. Fairfax[1], Matthew A. Williams[1,2], Sheri L. Holmen[2,3,8], Roger K. Wolff[1,2] & Allie H. Grossmann[1,2,3,10]

Tumour-host immune interactions lead to complex changes in the tumour microenvironment (TME), impacting progression, metastasis and response to therapy. While it is clear that cancer cells can have the capacity to alter immune landscapes, our understanding of this process is incomplete. Herein we show that endocytic trafficking at the plasma membrane, mediated by the small GTPase ARF6, enables melanoma cells to impose an immunosuppressive TME that accelerates tumour development. This ARF6-dependent TME is vulnerable to immune checkpoint blockade therapy (ICB) but in murine melanoma, loss of *Arf6* causes resistance to ICB. Likewise, downregulation of *ARF6* in patient tumours correlates with inferior overall survival after ICB. Mechanistically, these phenotypes are at least partially explained by ARF6-dependent recycling, which controls plasma membrane density of the interferon-gamma receptor. Collectively, our findings reveal the importance of endomembrane trafficking in outfitting tumour cells with the ability to shape their immune microenvironment and respond to immunotherapy.

Immune escape, a hallmark of cancer[1], involves cancer cell sensing and direct disarming of immune attack. Cancer-cell intrinsic mechanisms of immune escape broadly include 1) altering the immune landscape of the tumour microenvironment (TME), 2) direct and indirect inhibition of CD8+ T cell effector function, and 3) altering tumour antigen expression or presentation (reviewed in refs. 2,3). The TME can be composed of diverse cell types that influence disease progression and response to therapy[4]. Given the performance and potential of immunotherapy, understanding how tumour cells impose changes on the immune system may improve rational clinical use of current immune checkpoint blockade (ICB) therapies and facilitate the development of new, immune-modulating drugs.

In melanoma, emerging evidence supports that a complex TME forms surprisingly early in tumour development[5]. In a small set of patient samples that ranged from atypical melanocytic proliferations to vertically invasive primary tumours, cytotoxic T lymphocytes (CTLs)

A full list of affiliations appears at the end of the paper. e-mail: allie.grossmann@providence.org

were detected with regulatory T cells (Tregs) and myeloid cells in precursor lesions, and the density of these cells increased with progression to melanoma in situ (antecedent to invasion). At the invasive stage, cytokine gradients decorated the TME, which had evolved into complex geospatial microenvironments representing multiple mechanisms of immune suppression, including IFNγ-dependent and independent pathways. These findings suggest that newly transformed melanoma cells may have an innate ability to launch immune evasive programmes and create an immunosuppressive TME.

Primary cutaneous melanomas are frequently infiltrated by lymphocytes to varying degrees, and dense infiltration is a favourable prognostic histopathologic feature[6]. Despite the immune surveillance, tumour-intrinsic machineries that might ensure nascent melanoma cells are equipped to adapt to immune editing are poorly understood. This is an important distinction because melanoma has an unusually high proclivity for early metastasis, when primary tumours are as thin as one millimetre[7], indicating that the behaviour of melanoma in early development is tightly linked to metastatic progression. Hence, this is a disease where understanding tumour-intrinsic mechanisms of immune escape during early-stage disease could lead to effective clinical interventions for this common, aggressive cancer.

During immune editing, cancer cells are exposed to a barrage of insults including Interferon gamma (IFNγ), Interferon alpha (IFNα), Tumour Necrosis Factor alpha (TNFα), lytic granules and death receptor ligands, released by CTLs and natural killer cells[8]. First contact with these assaults occurs at the tumour cell plasma membrane. In general, plasma membranes are dynamic interfaces where the repertoire of proteins and lipids is remodelled by the endomembrane trafficking system in response to changing environments and cellular needs[9]. Endomembrane trafficking machineries is responsible for internalizing plasma membrane proteins and directing them towards being secreted, recycled to the cell surface, or degraded in lysosomes. Given the rush of cytokines released during immune attack, endomembrane trafficking machinery might mediate the dynamic responses of cancer cells by controlling the density of cytokine receptors, or other key proteins, at the cell surface. At present, our understanding of this process is limited by a lack of in vivo models that directly interrogate trafficking genes in immunocompetent hosts.

The small GTPase ADP-Ribosylation Factor 6 (ARF6) localizes to the plasma membrane and has been reported to mediate endocytosis and recycling of plasma membrane proteins[10–13]. ARF6 is activated by and coordinates signalling, cargo transport and functional output of diverse ligand-receptor systems[14–21]. In addition, ARF6 is upregulated and/or activated downstream of oncoproteins such as mutant GNAQ[22], p53 and KRAS[23]. Like other small GTPases, activation of ARF6 by GTP loading is mediated by guanine exchange factors (GEFs), while conversion of active ARF6-GTP to inactive ARF6-GDP is catalysed by GTPase activating proteins (GAPs) (Fig. 1a). Thus, GEFs and GAPs determine the lifespan of ARF6 activation and an imbalance in expression of these proteins could shift the activation-deactivation cycle of ARF6 to favour one state over the other. We reported that reduced expression of ARF6 GAPs (*ACAP1 and ARAP2*), in metastatic melanoma from Stage III patients, was associated with inferior overall survival[24]. We also showed that ARF6-GTP levels were aberrantly high in metastatic melanoma, compared to adjacent benign tissues, and that ARF6 activation accelerated spontaneous metastasis in xenografts and genetically engineered tumour models[15,24]. Specifically, ARF6-GTP in primary tumours promoted metastasis without increasing primary tumour growth. Likewise, pharmacologic inhibition of ARF6 reduced spontaneous metastasis without altering primary tumour growth in an immunodeficient model of cutaneous melanoma[15]. These results can be partly attributed to the pro-invasive functions of ARF6 that we and others have reported[15,24], however, this may not fully explain the pro-metastatic roles of ARF6. Successful metastasis requires much more than the acquisition of invasive behaviour; it also requires immune escape during primary tumour development.

Here, we show that tumour-intrinsic ARF6 promotes primary tumour development in an immunocompetent host. Upon melanocyte-specific, inducible deletion of the *Arf6* gene simultaneously with oncogenic BRAF activation and *Cdkn2a* deletion, we report that tumourintrinsic ARF6 restricts adaptive immunity during melanoma development and is responsible for broad changes in the local tumour immune landscape. These ARF6-dependent changes to the TME ultimately render tumours vulnerable to ICB therapy. In both murine and human cancer cells, ARF6 maintains IFNγ receptor density in the plasma membrane, leading to a cascade of immunosuppressive output that helps remodel the TME. The work herein demonstrates the critical nature of ARF6 endomembrane trafficking in equipping tumour cells with an innate ability to execute immune resistance programmes that accelerate tumour development but that are susceptible to ICB. Our combined data support downregulation of *ARF6* expression and activation as a mechanism of resistance to ICB therapy in melanoma patients.

Results

Loss of ARF6 restricts primary melanoma formation and progression

Similar to our previous analysis of The Cancer Genome Atlas (TCGA) metastatic melanomas[24], we interrogated expression of all *ARF* gene family members, as well as ARF6 GEF and GAP genes (Supplementary Table 1) in primary tumours from the Leeds Melanoma Cohort, which includes over 700 primary melanomas from Stage I-III, treatment naïve patients[25]. While *ARF6* was not present in the tumour gene expression dataset, high expression of ARF6 GAP genes, predicted to inactivate ARF6 in these primary tumours, significantly correlated with superior overall survival of both Stage II and Stage III patients (Fig. 1b), similar to metastatic melanoma[24]. The prognostic GAP genes include *ACAP1*, an ARF6 GAP[26–28], and *ASAP3*, an ARF1/ARF5/ARF6 GAP[29]. Purified ACAP1 has been reported to have selective GAP activity for ARF6 over ARF1 or ARF5[26]. Interestingly, *ACAP1* is prognostic in both primary (Leeds cohort, Fig. 1b) and metastatic (TCGA cohort)[24] disease, and ectopic expression of ACAP1 inactivated ARF6 (reduced ARF6-GTP level) in human cutaneous melanoma cells (Fig. 1c), consistent with previous studies in other cell lineages[27,28]. Overall, these data suggest that variable expression of ACAP1 in primary melanoma (Fig. 1b) impacts the activation level of ARF6 (Fig. 1c) and can influence both primary and metastatic disease progression.

To investigate a role for ARF6 in the initiation and propagation of primary melanoma in vivo, we crossed $Arf6^{flox/flox}$ ($Arf6^{f/f}$) mice[30] with *Dct::TVA; Braf*^{V600E}*; Cdkn2a*$^{f/f}$ mice and induced genetic alterations specifically in melanocytes via subcutaneous injection of RCAS-Cre into the flank, as previously described[31]. In this model, loss of *Arf6* significantly reduced tumour incidence (Fig. 1d), increased disease latency (Fig. 1e), slowed tumour growth, which was measured from the time of tumour formation (Fig. 1f), and prolonged host survival (Fig. 1g). Interestingly, Western blot of primary tumour cell lines showed that up to 30% of the $Arf6^{f/f}$ tumours retained a comparatively low level of ARF6 expression (Supplementary Fig. 1a). Among the ARF family of proteins, ARF6 uniquely localizes and functions at the cell periphery[32] but has overlapping and synergistic roles with ARF1[33]. Notably, in ARF6 knockout cells, expression of ARF1 remained intact (Supplementary Fig. 1a). Thus, it is possible that in a fraction of the $Arf6^{f/f}$ mice, $Arf6^{WT}$ tumour subclones may exist due to incomplete Cre-mediated recombination of the $Arf6^{f/f}$ allele. Alternatively, there may be persistent non-tumour cells in these early passage cultures. In situ hybridization detected reduced, heterogeneous *Arf6* mRNA signals in whole tumour sections (tumour + intact stroma) from $Arf6^{f/f}$ mice (Supplementary Fig. 1b). While low expression of *Arf6* may have persisted in a minor fraction of the $Arf6^{f/f}$ cohort, there is a significant

https://doi.org/10.1038/s41467-024-50881-1

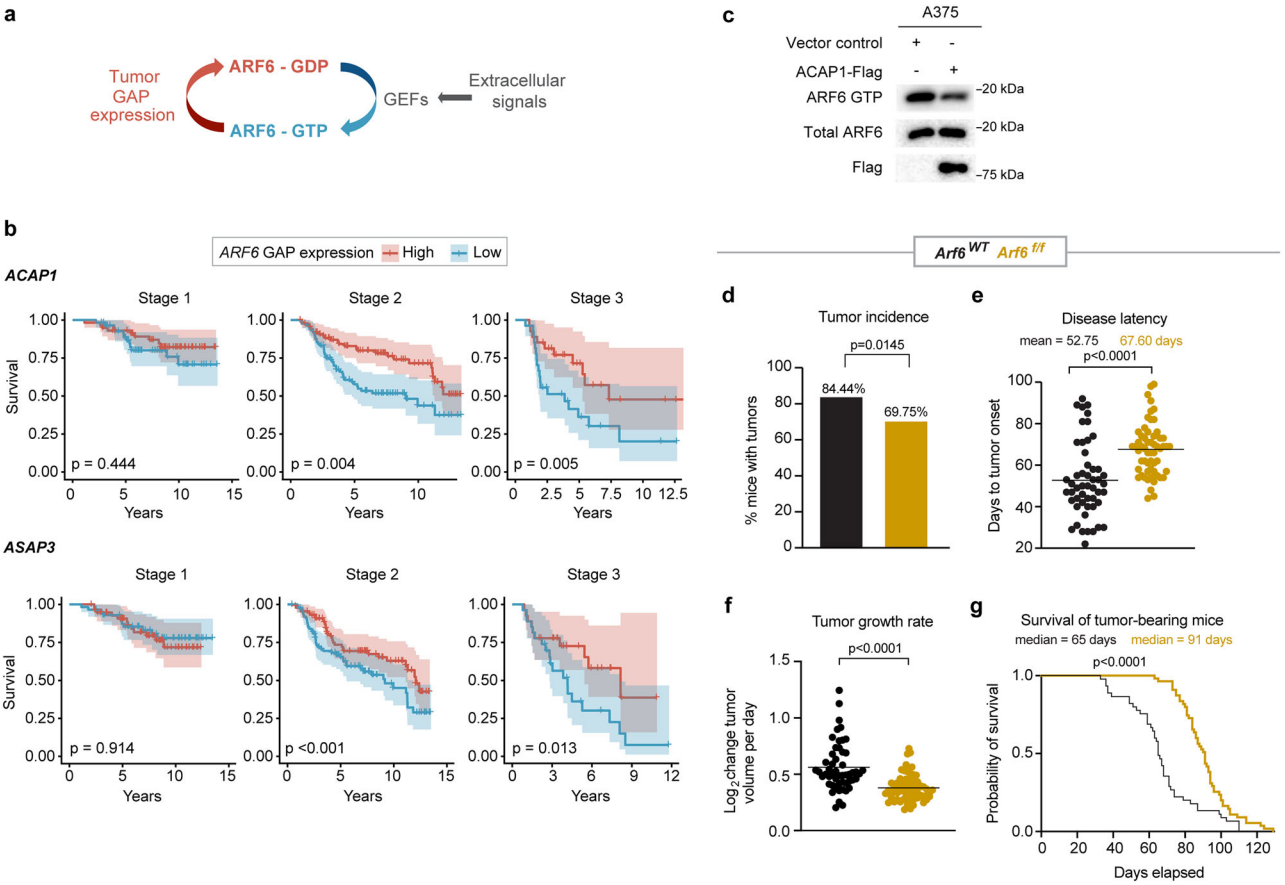

Fig. 1 | ARF6 promotes primary melanoma formation and progression. **a** Schematic diagram showing ARF6 cycles between the GDP-bound inactive form (red) and the GTP-bound active form (blue). **b** Correlations between the top and the bottom quartile of mRNA expression levels of indicated ARF6 GAPs in primary cutaneous melanoma (the Leeds cohort) with survival of patients, stage I $n = 58$, stage II $n = 88$, and stage III $n = 26$ in each high and low cohort, p values from Cox proportional hazards regression model. **c** Total ARF6 and ARF6-GTP pulldown in A375 human melanoma cells with or without ectopic ACAP1 expression, $n = 1$ experiment. **d**–**g** Melanocyte-specific deletion of *Arf6* restricts tumourigenesis. **d** Percent of *Dct::TVA; Braf*^{V600E}*; Cdkn2a*$^{f/f}$ mice that developed tumours within 100 days after Cre injection (tumour induction). $n = 90$ *Arf6* wild-type (*Arf6*^{WT}), $n = 119$ *Arf6* floxed (*Arf6*$^{f/f}$), two-sided Fisher's exact test. **e** Days to initial tumour detection after Cre injection, two-tailed t-test with Welch's correction. $n = 51$ *Arf6*^{WT}, $n = 58$ *Arf6*$^{f/f}$ mice. **f** Rate of tumour growth measured from time of initial detection, $n = 52$ *Arf6*^{WT}, $n = 68$ *Arf6*$^{f/f}$ mice. **g** Survival of mice (before primary tumour reached 2 cm) after Cre injection (day 0) within 130 days, $n = 45$ *Arf6*^{WT}, $n = 54$ *Arf6*$^{f/f}$ mice, Log-rank (Mantle-Cox) test. See also Supplementary Fig. 1. **e**–**f** Solid line within data points = mean. Source data are provided as a Source Data file.

defect in tumour development and growth in this population (Fig. 1d–g). No significant differences in tumourigenesis, nor progression, were observed between sexes (Supplementary Fig. 1c). In addition, early passage murine melanoma cell lines showed no significant difference in proliferation between genotypes (Supplementary Fig. 1d). This is consistent with our previous findings in this model whereby tumour-specific expression of ARF6^{Q67L}, a constitutively active (GTP-bound) form of ARF6, accelerated spontaneous metastasis without increasing primary tumour development, proliferation, or growth in this model[24]. Overall, the phenotypes of these models may reflect distinct functions for ARF6 during tumour progression that depend on expression level and/or activation state.

Loss of ARF6 enhances tumour inflammation and apoptosis

To explore potential mechanisms of ARF6-dependent tumour development, we analyzed pathway alterations using bulk transcriptomes from murine tumours expressing constitutively active ARF6^{Q67L} (phenotype previously published[24]) or deleted *Arf6* (ARF6$^{f/f}$), each compared to wild-type ARF6 (ARF6^{WT}) tumours. Strikingly, ARF6^{Q67L} and ARF6$^{f/f}$ tumours shared several Hallmark gene sets, with opposite directions of enrichment (Supplementary Fig. 1e, f), highlighted by significantly decreased expression of IFNα, IFNγ and TNFα signatures in ARF6^{Q67L} tumours but enrichment of these in ARF6$^{f/f}$ tumours (Fig. 2a). These cytokine signatures suggest that ARF6 may control the ability of tumours to shape their immune microenvironment. Histologically, tumour infiltrating lymphocytes (TIL) were scattered diffusely in the ARF6^{WT} tumours and formed subtle, small clusters rarely; in contrast, the TIL in ARF6$^{f/f}$ tumours formed obvious, robust clusters, and were evident in significantly more mice (Fig. 2b). In addition, compared to ARF6^{WT}, ARF6$^{f/f}$ tumours showed significantly decreased levels of phosphorylation of death-associated protein kinase 1 (DAPK1) at serine 308, which is reported to initiate IFNγ-induced apoptosis[34], and increased levels of cleaved executioner caspases 3 and 7 (Fig. 2c), indicating increased apoptosis. Importantly, consistent with murine tumours, primary human melanomas with high expression of ARF6 GAPs, which are predicted to have relatively low ARF6-GTP levels, showed significant enrichment in tumour-infiltrating immune cells, particularly cytotoxic CD8+ T cells, compared to tumours with low expression of ARF6 GAPs (Fig. 2d). These data together support that the overall level of ARF6 activation in tumour cells may have regulated an antitumour immune response.

Tumour-intrinsic ARF6 inhibits CTL function and recruits pro-tumourigenic immune cells

To determine how ARF6 might alter the TME, we profiled the immune cells in ARF6^{WT} and ARF6$^{f/f}$ tumours using flow cytometry.

https://doi.org/10.1038/s41467-024-50881-1

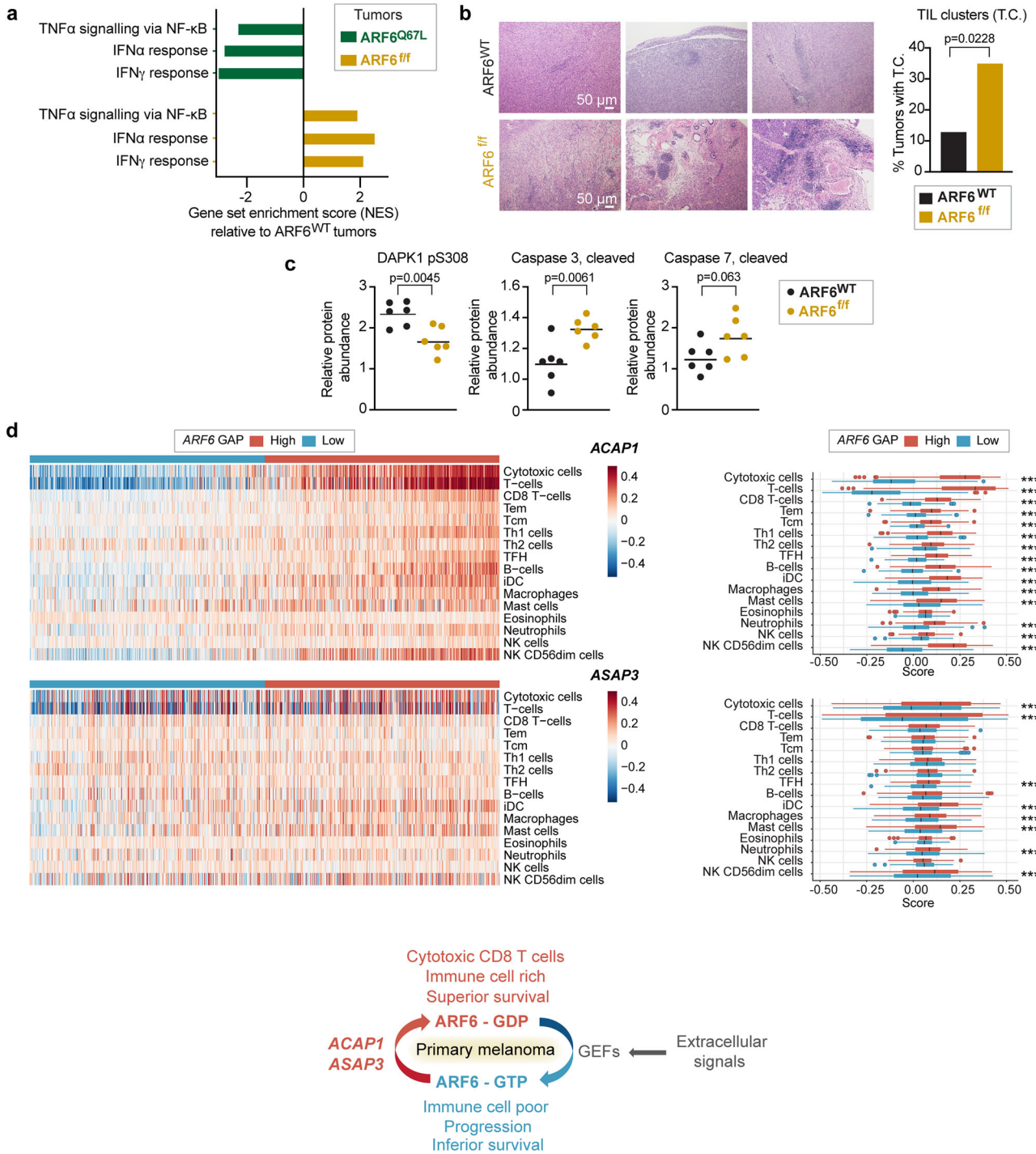

Fig. 2 | ARF6-dependent tumour inflammation and apoptosis. a Shared significantly enriched gene sets (MSigDB Hallmark), but in opposite directions, between ARF6$^{f/f}$ and ARF6^{Q67L} tumours from bulk tumour transcriptomes ($n = 6$ ARF6$^{f/f}$ vs. $n = 6$ ARF6^{WT} tumours, $n = 6$ ARF6^{Q67L} vs. $n = 4$ ARF6^{WT} tumours). See also Supplementary Fig. 1e, f. **b** Representative images of H&E staining showing clusters of small round blue cells, i.e., tumour-infiltrating lymphocytes (TIL) clusters, scale bars = 50 µm, and fractions of tumours with TIL clusters ($n = 46$ ARF6^{WT} controls, $n = 40$ ARF6$^{f/f}$ tumours), Fisher's exact test, two-sided. **c** Apoptotic protein profile of tumours ($n = 6$ mice each) detected by Reverse Phase Protein Array, two-tailed *t*-test. Solid line within data points = geometric mean. **d** Immune cell gene set enrichment in primary human melanoma (Leeds melanoma, $n = 350$), supervised clustering with ARF6 GAP expression (related to Fig. 1b). The box corresponds second and third quartiles. The middle horizontal line = median. Dots are outlier further than 1.5 * IQR (inter-quartile range). ***$p < 0.001$. *ACAP1* cytotoxic T cells $p = 9.924 \times 10^{-124}$, T cells $p = 2.636 \times 10^{-141}$. *ASAP3* cytotoxic T cells $p = 2.7081 \times 10^{-8}$, T cells $p = 1.2997 \times 10^{-8}$. two-tailed *t*-test. Schematic = ARF6 activation cycle related to ARF6 GAP expression detected in primary tumours, and associated immune cell signatures and survival outcome. See also Supplementary Fig. 1c, d. Source data are provided as a Source Data file.

While the absolute number of CD45+ immune cells was slightly reduced in ARF6$^{f/f}$ tumours, no significant difference was observed in the fractions of CD4+ T cells, CD8+ T cells, B cells, macrophages, NK cells, or dendritic cells between ARF6^{WT} and ARF6$^{f/f}$ tumours (Supplementary Fig. 2a–d). Given that IFN signalling and TNFα signalling were increased in the TME of ARF6$^{f/f}$ tumours (Fig. 2a), we hypothesized that CD8+ T cells in ARF6$^{f/f}$ tumours could have enhanced antitumour activity. Indeed, ARF6$^{f/f}$ tumours showed

significantly higher percentages of IFNγ+ and granzyme B+ (GzmB+) CD8+ T cells (Fig. 3a, b), demonstrating enhanced CD8+ T cell effector function, which may explain why tumourigenesis and progression were limited without ARF6. There was no significant difference in CD8+ T cell effector function in spleens from *Arf6*$^{f/f}$ and *Arf6*^{WT} mice (Fig. 3a, b), indicating a localized effect within the TME. There was also no significant difference in PD-1 + CD8+ T cells in ARF6$^{f/f}$ tumours compared to ARF6^{WT} tumours (Fig. 3b). Interestingly, ARF6$^{f/f}$ tumours showed a significantly lower percentage of FoxP3+ Tregs and a lower Treg/CD8 ratio (Fig. 3c, d), consistent with alleviation of immune suppression.

To interrogate the TME in higher resolution, we subjected CD45+ tumour infiltrating immune cells to single-cell RNA sequencing (scRNA-seq) and found significant differences between genotypes (Fig. 3e). ARF6^{WT} tumours contained a prominent population of polymorphonuclear neutrophil-derived, myeloid-derived suppressor cells (MDSC-PMN), distinguished by expression of *Cd84*, *Arg2*, *Irf1*, *Nfkbiz*, *Il1b*, *Csf1*, and *Ptgs2*[35]. These MDSC-PMNs were largely absent from the ARF6$^{f/f}$ tumours. In addition, there appeared to be a significant shift in the differentiation of monocytes into macrophages in the ARF6$^{f/f}$ tumours. T cell clusters also showed significant differences between ARF6^{WT} tumours and ARF6$^{f/f}$ tumours. Whereas naïve-like CD8+ T cells dominated ARF6^{WT} tumours, effector memory and cytolytic (exhausted) T cells dominated ARF6$^{f/f}$ tumours (Fig. 3f), concordant with an increased effector function of CD8+ T cells in ARF6$^{f/f}$ tumours measured by flow cytometry (Fig. 3a, b) and the increased Interferon and TNFα signalling seen in the TME (Fig. 2a).

High proportions of CD11b+ myeloid cells were found in both ARF6^{WT} and ARF6$^{f/f}$ tumours (Supplementary Fig. 2c and Fig. 3g). Further analysis of this population revealed 12 clusters: five were macrophages, two each were granulocytes and myeloid dendritic cells, and one each was Sparc^{+} Spp1^{+} cells, NK cells and mast cells (Fig. 3g). Compared to ARF6^{WT} tumours, ARF6$^{f/f}$ tumours exhibited an increased fraction of macrophage clusters (macrophages I to V), a decreased fraction of granulocyte clusters (granulocytes I to II) and an expansion of myeloid dendritic cells. Within the five macrophage clusters, expression of IFNγ-inducible genes, such as MHC class II and Fc gamma receptor, were higher in ARF6$^{f/f}$ tumours (Supplementary Fig. 2e, Supplementary Table 2), which was consistent with the higher IFNγ production observed in CD8+ T cells from ARF6$^{f/f}$ tumours (Fig. 2a). Expression of efferocytosis-related genes was variable between genotypes and there was no clear trend (Supplementary Fig. 2e). Overall, these data suggest heightened antigen presentation and opsonic phagocytosis by macrophages in the ARF6$^{f/f}$ TME.

Both the flow cytometry (Fig. 3a–d) and scRNA-seq (Fig. 3f) findings indicated a heightened antitumoural immune response mediated by CD8+ T cells. To confirm that the growth of ARF6$^{f/f}$ tumours was restricted by the adaptive immune response, we treated *Arf6*$^{f/f}$ mice with anti-CD8 antibody to deplete CD8+ T cells. This resulted in efficient removal of CD8+ T cells in spleen and tumour tissues (Supplementary Fig. 3a, b) and significantly accelerated tumour progression (Fig. 3h). Unlike the *Arf6*$^{f/f}$ mice, tumour progression was unaffected by CD8 depletion in *Arf6*^{WT} mice (Supplementary Fig. 3c, d), consistent with Fig. 3b showing that CD8+ T cell effector function was suppressed in ARF6^{WT} tumours. These results confirmed that CD8+ T cells restricted tumour progression in *Arf6*$^{f/f}$ mice and that ARF6 was critical for tumour-mediated suppression of the adaptive immune response. In fact, CD8+ T cell depletion in *Arf6*$^{f/f}$ mice restored tumour growth to a rate equivalent to untreated *Arf6*^{WT} mice (Supplementary Fig. 3d). Overall, our combined data demonstrates that loss of ARF6 in tumours leads to an immune permissive TME and heightened CTL function.

Tumours with low ARF6 expression are insensitive to ICB

Given the opposite IFNγ signalling profiles observed between ARF6^{WT} and ARF6$^{f/f}$ tumours, (Fig. 2a), we asked whether tumourintrinsic ARF6 might impact response to ICB therapy. IFNγ in the TME elicits adaptive expression of immunosuppressive genes from cancer cells, including *CD274* (encoding PD-L1), *CD80* and *IDO1* (Indoleamine 2, 3-dioxygenase 1)[36–38]. PD-L1 and CD80 are immune checkpoint ligands for PD-1 and CTLA-4 receptors, respectively, expressed on CTLs. ICB specifically targets IFNγ-mediated immune suppression by blocking binding of PD-L1 or CD80 to their receptors, restoring the effector function of CTLs. We treated *Arf6*^{WT} and *Arf6*$^{f/f}$ mice with systemic anti-PD-1 antibodies just prior to mean tumour onset/palpable tumour detection. Anti-PD-1 treatment significantly limited tumour development in *Arf6*^{WT} mice (Fig. 4a). Tumour growth was also restricted in *Arf6*^{WT} mice when treatment was initiated after tumours were well established (Supplementary Fig. 4a). Consistent with this disease control, anti-PD-1 therapy significantly increased CD8+ T cell effector function (Supplementary Fig. 4b). These data confirm that in our BRAF^{V600E} melanoma model, tumour initiation and progression were significantly reliant on PD-L1-mediated immune suppression. In stark contrast, anti-PD-1 treatment failed to alter tumour development in *Arf6*$^{f/f}$ mice (Fig. 4a), failed to limit growth of established tumours (Supplementary Fig. 4a), and failed to boost CD8+ T cell effector function (Supplementary Fig. 4b). Resistance to anti-PD-1 therapy in *Arf6*$^{f/f}$ mice suggests a defect in PD-L1-mediated immune suppression by cancer.

Next, we asked whether there was evidence of ARF6-dependent, IFNγ-driven immune suppression in clinical specimens. We hypothesized that the expression level of *ARF6* in patient tumours might correlate with responses to ICB. Cancer-Immu analysis of integrated data from 13 melanoma cohorts[39] showed that the overall expression of *ARF6* in pretreatment tumour biopsies was heterogeneous among patients with advanced-stage melanoma treated with ICB and that the level of *ARF6* in these tumours significantly correlated with ICB outcomes (Fig. 4b). Specifically, patients whose tumours expressed low levels of *ARF6* had inferior overall survival after ICB compared to those whose tumours expressed high levels of *ARF6* (Fig. 4b). This was also true for the ARF6 GEF *CYTH1* (Supplementary Fig. 4c), which similar to ARF6, localizes to the plasma membrane[40]. As expected, *CYTH-1* knockdown reduced the level of ARF6-GTP in melanoma cells (Supplementary Fig. 4d). Supplementary Table 3 lists the statistical values of all ARFs, GAPs and GEFs interrogated. *CYTH4* expression also correlated with superior outcome (Supplementary Fig. 4e), although this GEF is specific for ARF1 and ARF5, rather than ARF6, and its expression is limited to leucocyte lineages, including T cells[41,42]. Thus, *CYTH4* expression likely reflects tumour infiltrating immune cells in these melanoma samples. Consistent with this, expression of lineage markers for CD4+ and CD8+ T cells, CD11c+ dendritic cells and CD11b+ macrophages, also correlate with superior survival (Supplementary Fig. 4f–i). Within the ARF family, ARF1 has distinct but similar functions as ARF6 and has been reported to cooperate with ARF6 in some scenarios[33]. Nevertheless, ARF1 does not localize to the plasma membrane or recycling endosomes like ARF6[40] and therefore, would not be expected to have a role in remodelling the landscape of immune-modulating plasma membrane proteins. Thus, it is pertinent that *ARF1* expression in melanoma did not associated with ICB treatment outcomes (Supplementary Fig. 4j).

Low expression of the ARF6 GAP *ACAP1* in tumours also associated with inferior survival with ICB therapy (Supplementary Fig. 4k). *ACAP1* localizes to recycling endosomes and reduced expression might enhance ARF6 activation during endocytic trafficking, however, reduced *ACAP1* expression was prognostic in both primary (Fig. 1b) and metastatic tumours[24], correlating with inferior survival of treatment-naïve patient cohorts[25,43]. Therefore, *ACAP1* expression in the ICB-treated cohorts likely reflects the prognostic status of this gene. In contrast, *ARF6* and *CYTH1* were not prognostic in untreated, TCGA[43], patients (Supplementary Fig. 4l): rather, their expressions were predictive of ICB treatment response, (Fig. 4b,

https://doi.org/10.1038/s41467-024-50881-1

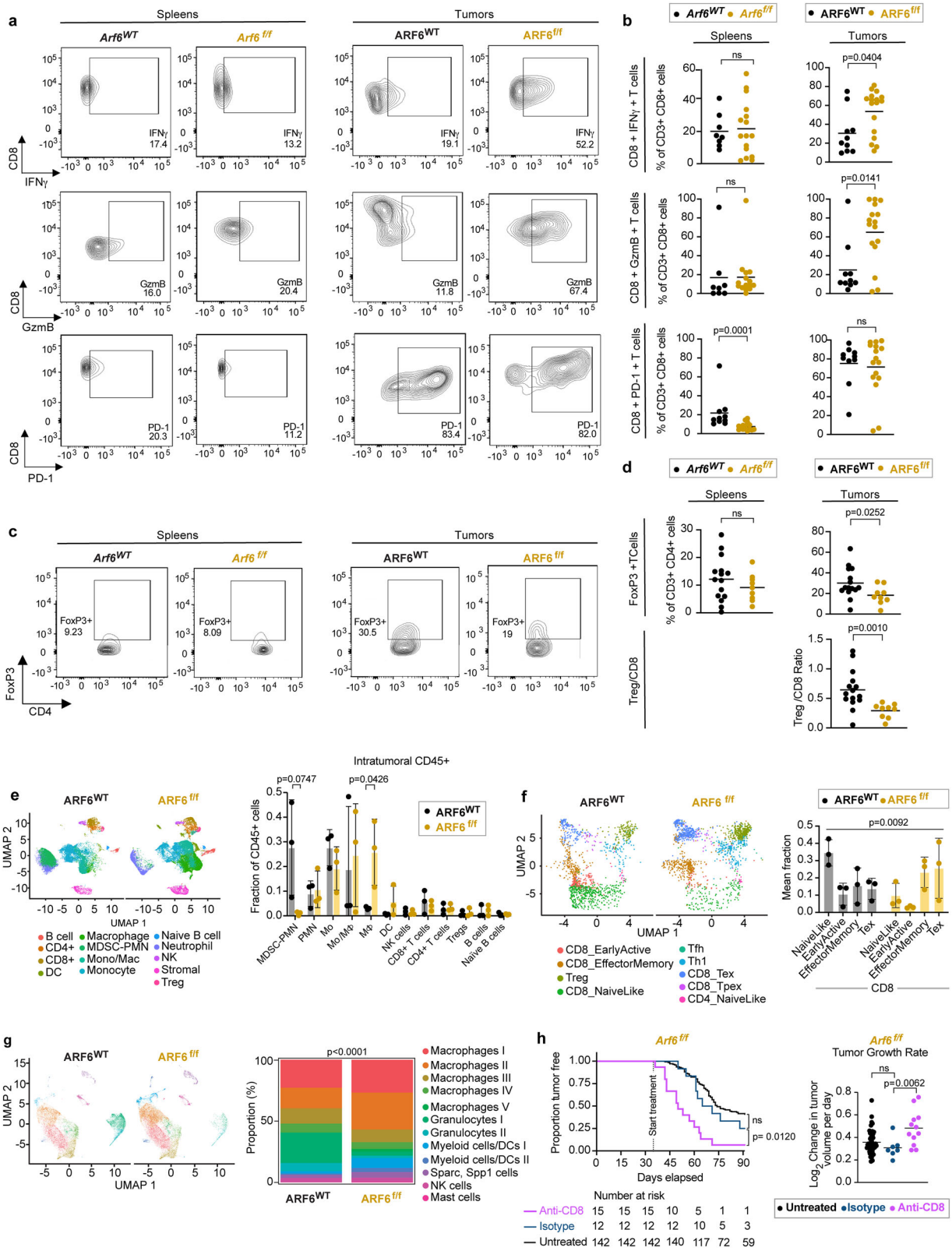

Supplementary Fig. 4c). Thus, downregulation of *ARF6* and *CYTH1* expression may yield relatively low, tumour intrinsic ARF6-GTP, potentially altering the plasma membrane protein dynamics during immune editing. Similarly, low expression of the IFNγ-inducible immunosuppressive genes *CD274* (encodes PD-L1) and *IDO1* were also predictive of inferior survival of ICB-treated patients (Supplementary Fig. 4m, n).

IFNγ-driven adaptive immune resistance requires ARF6

Because tumour-specific deletion of *Arf6* increased IFN signalling in the TME (Fig. 2a) and CD8+ T cell-mediated immunity (Fig. 3), we interrogated the immunosuppressive output of IFNγ signalling in tumour cells. First, we used immunohistochemistry (IHC) to analyze the PD-L1 expression in situ. PD-L1 was present in a heterogeneous, multifocal pattern in the majority (70%) of ARF6^{WT} tumours tested

https://doi.org/10.1038/s41467-024-50881-1

Fig. 3 | Heightened anti-tumour immunity in ARF6$^{f/f}$ tumours. a Flow cytometry charts and (**b**) quantification of IFNγ (spleens: *Arf6*^{WT} $n = 8$, *Arf6*$^{f/f}$ $n = 16$; tumours: ARF6^{WT} $n = 10$, ARF6$^{f/f}$ $n = 17$), granzyme B (GmzB) (spleens: *Arf6*^{WT} $n = 8$, *Arf6*$^{f/f}$ $n = 15$; tumours: ARF6^{WT} $n = 10$, ARF6$^{f/f}$ $n = 16$) and PD-1(spleens: *Arf6*^{WT} $n = 10$, *Arf6*$^{f/f}$ $n = 15$; tumours: ARF6^{WT} $n = 10$, ARF6$^{f/f}$ $n = 16$ in CD8+ T cells from spleens and tumours of mice bearing ARF6^{WT} or ARF6$^{f/f}$ tumours upon T cell reactivation), two-tailed Mann Whitney test. **c** Flow charts and (**d**) quantification of the CD4+ FoxP3+ regulatory T cell fraction from spleens and tumours (spleens: *Arf6*^{WT} $n = 15$, *Arf6*$^{f/f}$ $n = 9$; tumours: ARF6^{WT} $n = 15$, ARF6$^{f/f}$ $n = 19$) of mice bearing ARF6^{WT} or ARF6$^{f/f}$ tumours and Treg/CD8 ratio (tumours: ARF6^{WT} $n = 15$, ARF6$^{f/f}$ $n = 19$), two-tailed Mann Whitney test. **e** Uniform manifold approximation and projection (UMAP) (scRNA-seq) showing intratumoural CD45+ cells ($n = 19{,}367$ cells from ARF6^{WT}, $n = 28{,}003$ cells from ARF6$^{f/f}$ tumours, $n = 3$ tumours of each genotype) and histogram showing mean % of immune cell types among total CD45+ cells. Unpaired *t*-tests Two-stage step-up (Benjamini, Krieger, and Yekutieli). **f** UMAP showing projection of T cell clusters onto ProjecTILs reference and histogram showing mean % of CD8 T cell subtypes among total CD8+T cells. ($n = 1402$ cells from ARF6^{WT}, $n = 1661$ cells from ARF6$^{f/f}$, $n = 3$ tumours of each genotype) Likelihood ratio test, mixed effects model with fixed group effect and random effect for samples within groups. Two-way ANOVA with Sidak's multiple comparisons tests (**g**) UMAP showing tumour infiltrating myeloid cells and stacked histogram showing proportion of each cell type (%) ($n = 12{,}295$ cells from ARF6^{WT}, $n = 13{,}807$ cells from ARF6$^{f/f}$ tumours, $n = 3$ tumours of each genotype). Two-sided chi-square test of homogeneity. **h** Tumour-free survival (Two-sided Kaplan–Meier log-rank test) and rate of tumour growth (untreated $n = 50$, isotype $n = 7$, anti-CD8 $n = 12$), Two-tailed Welch's *t*-test, *Arf6*$^{f/f}$ mice with or without CD8 T cell depletion. Antibody treatments were initiated when mice were 5 weeks old and continued for 8 weeks. See also Supplementary Figs. 2 and 3. **b**, **d**, **h** Solid line within data points = mean. **e**–**f** Solid line within data points = mean. Error bars = SD. Source data are provided as a Source Data file.

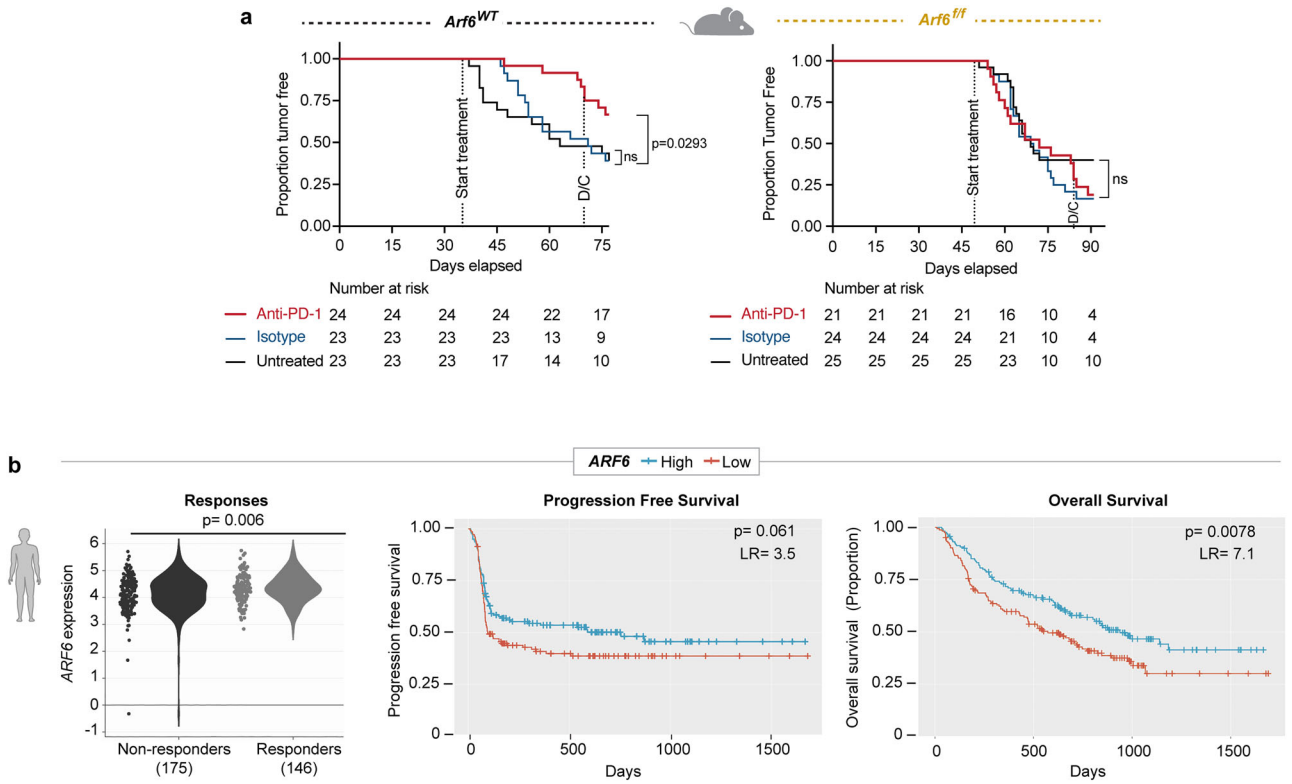

Fig. 4 | ARF6 status in tumours distinguishes ICB outcomes. a Systemic anti-PD-1 treated for 5 weeks duration. Includes mice that developed tumours within 35–77 (*Arf6*^{WT}) days or 49–91 (*Arf6*$^{f/f}$) days after Cre injection. Kaplan–Meier log-rank test. D/C = discontinued treatment. **b** Association of ICB treatment outcome with mRNA levels of *ARF6* in transcriptomes of pretreatment melanoma biopsies (Cancer-Immu expression analysis, aggregated data from $n = 13$ queried melanoma clinical studies, adjusted *p*-values, Benjamini and Hochberg procedure, LR = likelihood ratio with df = 1, PFS $n = 140$, OS $n = 160$ in each high and low cohort). See also Supplementary Fig. 4. Source data are provided as a Source Data file.

whereas it was undetectable by IHC in ARF6$^{f/f}$ tumours (Fig. 5a), despite heightened IFNγ signalling detected in the TME (Fig. 2a). In vitro, both ARF6^{WT} and ARF6$^{f/f}$ murine melanoma cells increased the expression of total and cell surface PD-L1 after exposure to IFNγ but ARF6$^{f/f}$ cells expressed significantly less of both (Fig. 5b, c). *CD274* (PD-L1) mRNA expression has been reported to peak between 6–12 h after the start of IFNγ treatment in human lung cancer cells[44]. In keeping with this time course, expression of *Cd274* was readily detectable in murine melanoma within 8 h of IFNγ treatment (Fig. 5d). Although ARF6 could potentially control the trafficking of PD-L1[23], *Cd274* expression after IFNγ exposure was ARF6-dependent (Fig. 5d). Likewise, in human melanoma cells, *ARF6* knockdown abrogated IFNγ-induced PD-L1 expression (Fig. 5e). In contrast, pharmacologic activation of ARF6 with the ARF GAP inhibitor QS11 significantly increased PD-L1 expression (Supplementary Fig. 5a).

In addition to PD-L1, ARF6$^{f/f}$ tumour cells expressed lower levels of CD80 before and after IFNγ treatment, compared to ARF6^{WT} cells (Fig. 5f). Likewise, IFNγ-induced IDO1 protein and mRNA expression were compromised by deletion or silencing of ARF6 (Fig. 5f, g, h). IDO1-dependent catalysis of tryptophan generates kynurenine, inducing immunosuppressive Tregs[45], as well as recruiting and activating MDSCs[46]. Thus, reduced IFNγ-induced IDO1 could explain why there were significantly fewer Tregs and MDSCs in ARF6$^{f/f}$ tumours (Fig. 3d, e). In addition to immunosuppressive genes, IFNγ can also induce MHC Class I expression in melanoma to enhance tumour antigen presentation and immunogenicity[47,48]. IFNγ treatment raised the level of MHC Class I protein, on the surface of ARF6$^{f/f}$ tumour cells, similar to that of unstimulated ARF6^{WT} tumour cells (Supplementary Fig. 5b). Interestingly, despite the comparably lower levels of IFNγ-induced MHC I in ARF6$^{f/f}$ tumours, antitumour CD8+ T cell

https://doi.org/10.1038/s41467-024-50881-1

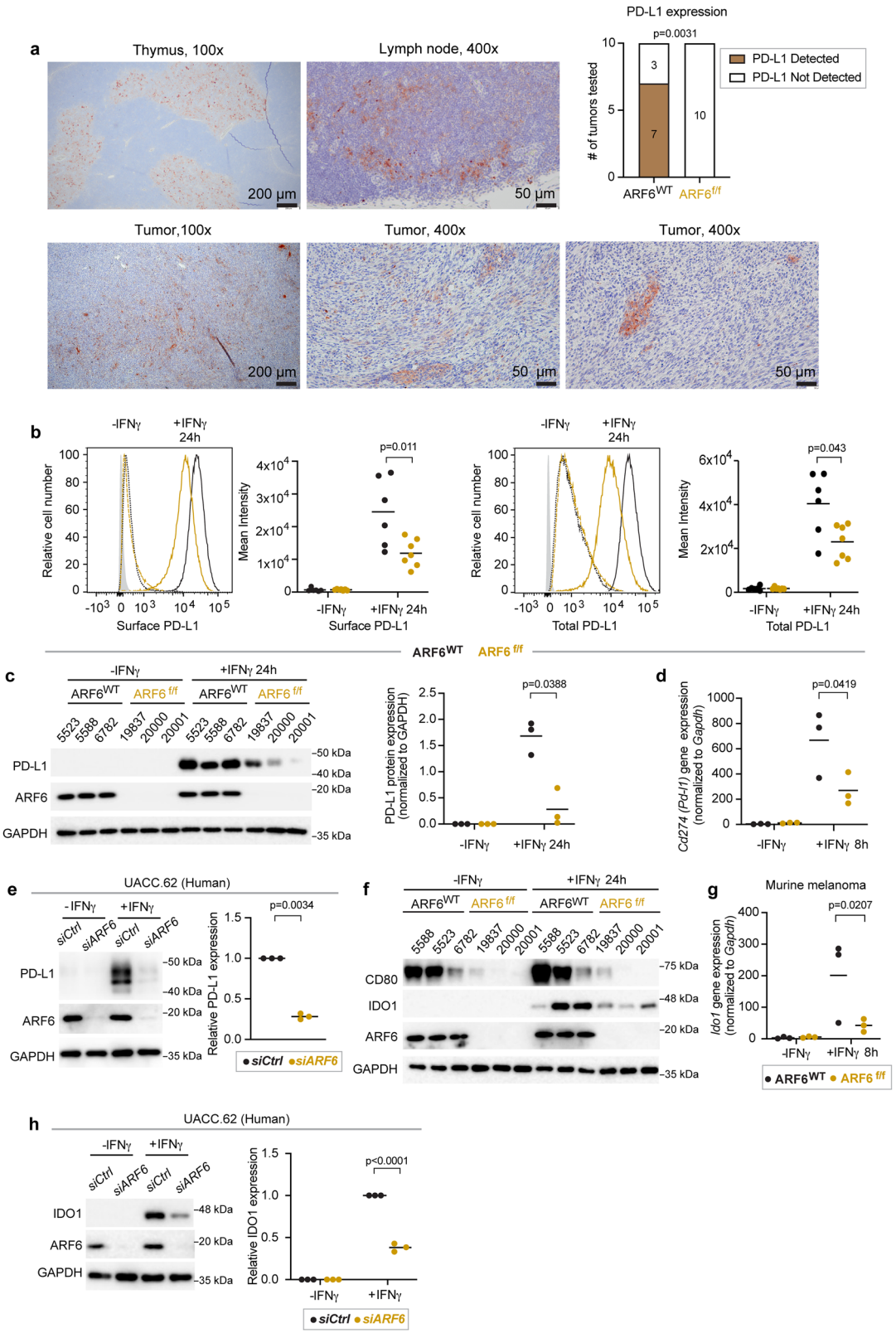

activity was heightened in the *Arf6*$^{f/f}$ mice (Fig. 3a, b, f, h). In contrast, expression of Gal3 and LSECtin, which are ligands of the immune checkpoint receptor LAG3 and are not IFNγ-inducible genes, were not dependent on ARF6 (Supplementary Figs 5c, d). Thus, ARF6-dependent expression of immunosuppressive genes is not a generalizable phenomenon.

ARF6 controls tumourintrinsic IFNγ signalling through trafficking of the IFNγR

With clear evidence of a heightened adaptive immune response and IFNγ signalling in the immune compartment of ARF6$^{f/f}$ tumours, we speculated that ARF6 may regulate tumour intrinsic IFNγ signalling. In principle, loss of ARF6 could alter endocytic trafficking of the IFNγ

Fig. 5 | Activation of ARF6 and expression of immunosuppressive genes downstream of IFNγ. a Representative images of immunohistochemical (IHC) detection of PD-L1 expression (brown) in ARF6^{WT} tumours and summary of PD-L1 detection in $n = 10$ tumours of each genotype tested, two-sided Fisher's exact test. Thymus and lymph node are used as controls, (**b**–**h**) IFNγ-induced expression. **b** Flow cytometric detection of tumour cell surface and total protein, ARF6^{WT} $n = 6$, ARF6$^{f/f}$ $n = 7$ biologically independent tumour cell lines of each genotype. **c** Western blot for indicated proteins, $n = 3$ biologically independent tumour cell lines of each genotype. **d** Quantitative RT-PCR analysis for *Cd274* mRNA, three biologically independent tumour cell lines of each genotype, $n = 3$ replicates per cell line, per treatment condition. **e** Western blot for indicated proteins in UACC.62 cells, $n = 3$ biologically independent experiments. **f** Western blot for indicated proteins in early-passage murine tumour cells, $n = 3$ biologically independent tumour cell lines of each genotype. **g** Quantitative RT-PCR for *Ido1* mRNA, $n = 3$ biologically independent tumour cell lines of each genotype, $n = 3$ replicates per cell line per condition. experiments. **h** Western blot for indicated proteins in UACC.62, $n = 3$ biologically independent experiments. **b**, **c**, **d**, **g** Two-way ANOVA with Tukey's multiple comparisons test. **e**, **h** Two-tailed, ratio paired *t*-test. **b**–**d**, **e**, **g**, **h** Solid line within data points = mean. See also Supplementary Fig. 5. Source data are provided as a Source Data file.

receptor (IFNγR), affecting surface expression of the receptor and responsiveness of tumour cells to IFNγ. To investigate these possibilities, we interrogated IFNγ induced JAK-STAT signalling in vitro. Early passage murine melanoma cells from ARF6$^{f/f}$ tumours showed a significantly reduced JAK1 and STAT1 phosphorylation after IFNγ stimulation (Supplementary Fig. 6a), suggesting that the overall strength of tumourintrinsic IFNγ signalling relies upon ARF6. Given the critical role of ARF6 in endocytic trafficking we hypothesized that ARF6 controls the surface expression of the IFNγ receptor. Indeed, cell surface and total levels of IFNγR1 were significantly reduced in ARF6$^{f/f}$ murine melanoma cells (Fig. 6a, b). However, the *Ifnγr1* mRNA level was similar between ARF6$^{f/f}$ and ARF6^{WT} tumour cells (Fig. 6c).

To test whether ARF6 controlled IFNγR1 protein levels in human tumours, we depleted ARF6 in early passage patient-derived melanoma cell lines and commercially available human melanoma cell lines. Partial knockdown of *ARF6* reduced the total IFNγR1 protein level in all of the human melanoma cells tested (Fig. 6d). Next, we asked whether this phenomenon was true in other cancers in which ICB is a standard of care therapy, i.e., cancers that rely on IFNγ-driven adaptive immune suppression and where IFNγR density at the cell surface might impact therapeutic outcome. Knockdown of *ARF6* in cell lines derived from non-small cell lung cancer (NSCLC), mismatch-repair deficient colorectal cancer (CRC) and triple-negative breast cancer (TNBC) similarly diminished the IFNγR1 protein level (Fig. 6e), supporting that ARF6-dependent regulation of IFNγR1 is conserved across cancer types. The total IFNγR1 protein level may, in fact, be tightly linked to the expression level of ARF6, as shown in Fig. 6f where partial knockdown of *ARF6* reduced the IFNγR1 protein by half in human melanoma cells. Consistent with murine cells, IFNγR1 localization at the cell surface in human tumour cells was diminished by ARF6 depletion (Fig. 6g). In contrast, activation of ARF6 with the ARF6 GAP inhibitor QS11[19,49] (Fig. 6h, Supplementary Fig. 6b) was sufficient to increase the total IFNγR1 protein level. Similarly, ectopic expression of ARF6^{Q67L} was sufficient to increase the total IFNγR1 protein level (Supplementary Fig. 6c), consistent with the effect of QS11 (Fig. 6h, Supplementary Fig. 6b) and confirming a specific role for ARF6-GTP in augmenting IFNγR1 protein level. QS11 also significantly increased surface expression of IFNγR1 (Supplementary Fig. 6d). Together these data provide evidence that the plasma membrane density and the total protein level of IFNγR1 in cancer cells depend on ARF6 expression and activity.

ARF6 is activated by interleukin 1β[19], Toll-like receptors[20,21], growth factor receptors[16,18,50–53], WNT-Frizzled[15,17], and numerous G-protein coupled receptors[14]. Nevertheless, activation of ARF6 by IFN receptors has not been reported. Importantly, IFNγ treatment significantly increased ARF6-GTP levels in murine and human melanoma cells (Fig. 6i). These data implicate ARF6 in a feedback loop that enhances IFNγR1 protein level, possibly by ARF6-mediated recycling of the receptor to the plasma membrane. Internalized plasma membrane proteins that are not recycled can be trafficked to the lysosome[9]. Thus, we hypothesized that loss of ARF6 would result in IFNγR1 trafficking to the lysosome for degradation. To explore this possibility, we first examined how IFNγR1 was degraded in melanoma. Inhibition of either lysosomal or proteasomal degradation increased the total amount of IFNγR1 protein and partially restored the IFNγR1 level upon the depletion of ARF6 (Fig. 6j). Hence, IFNγR1 protein stability is regulated by distinct mechanisms that may serve different cellular functions in tumour progression. Importantly, silencing *ARF6* led to significant enrichment of degraded IFNγR1 in the lysosomes (Fig. 6k). Given this occurred in the absence of IFNγ ligand, our data suggest that ARF6 may be critical for recycling the constitutively internalized pool of the IFNγR1. Supplementary Fig. 6e shows ligand-independent internalization of the IFNγR1. Pharmacologic inhibition of ARF6 with SecinH3[15] had no effect on IFNγR1 constitutive internalization (Supplementary Fig. 6f). In contrast, recycling of the receptor is compromised by inhibition of ARF6; seen as cytoplasmic retention of the receptor with SecinH3 treatment, compared to vehicle control (Supplementary Fig. 6g). These results are consistent with flow cytometry (Fig. 6a, g, Supplementary Fig. 6d) showing deletion and/or knockdown of ARF6 reduce surface IFNγR1 localization, whereas pharmacologic activation of ARF6 enriches surface IFNγR1 localization. Together these findings demonstrate that the endocytic pool of the IFNγR1 in tumour cells is regulated by ARF6. Without sufficient expression and activation of ARF6, the receptor is degraded in the lysosome and IFNγ-mediated adaptive immune suppression is compromised.

Discussion

Here, we report that the endocytic trafficking protein ARF6 promotes primary melanoma development (Fig. 1) by empowering tumour cells to change the composition of local immune cell populations (Figs. 3 and 7). ARF6 creates a TME that is vulnerable to ICB, whereas tumours that downregulate ARF6 expression and/or activation are resistant to anti-PD-1 therapy (Figs. 4, and 7, Supplementary Fig. 4). Our combined murine and human data suggest that the ARF6 activation level may function as an internal rheostat controlling immunosuppressive output of cancer cells. Treatment naïve melanomas may enhance ARF6 activation by downregulating expression of *ACAP1* (in primary, Fig. 1b, and metastatic tumours[24]), and by growth factor[14], WNT5A[15], or IFNγ signalling (Fig. 6i). Tumours that inactivate ARF6 by downregulating *ARF6* or *CYTH1* have an advantage during ICB by conferring therapy resistance (Fig. 4, Supplementary Fig. 4). Mechanistically, ARF6-mediated IFNγR1 trafficking can help explain both of these phenomena. When ARF6 is activated by IFNγ (Fig. 6i), melanoma cells are equipped with IFNγR at the plasma membrane (Fig. 6a, g) in sufficient quantities to support tumourintrinsic IFNγ signalling (Supplementary Fig. 6a) and downstream expression of immunosuppressive genes (Fig. 5) that directly inhibit CTLs and recruit MDSCs and Tregs (Figs. 3 and 7). Consequently, tumour-intrinsic ARF6 bolsters a TME that reduces differentiation of the monocyte/macrophage population into phagocytic, antigen-presenting cells that are characteristic of anti-tumour activity (Fig. 3 and Supplementary Fig. 2e). Overall, our data define a powerful mechanism of local immune modulation by cancer cells accomplished through ARF6-mediated endocytic trafficking (Fig. 7).

From seminal work by Celada and Schreiber[54], we learned that the amount of IFNγ internalization by cells depends on an intracellular pool of the receptor and an unknown mechanism of recycling. How the IFNγR1 receptor returns to the plasma membrane after endocytosis has remained a mystery until now. Our data-position ARF6 in this

https://doi.org/10.1038/s41467-024-50881-1

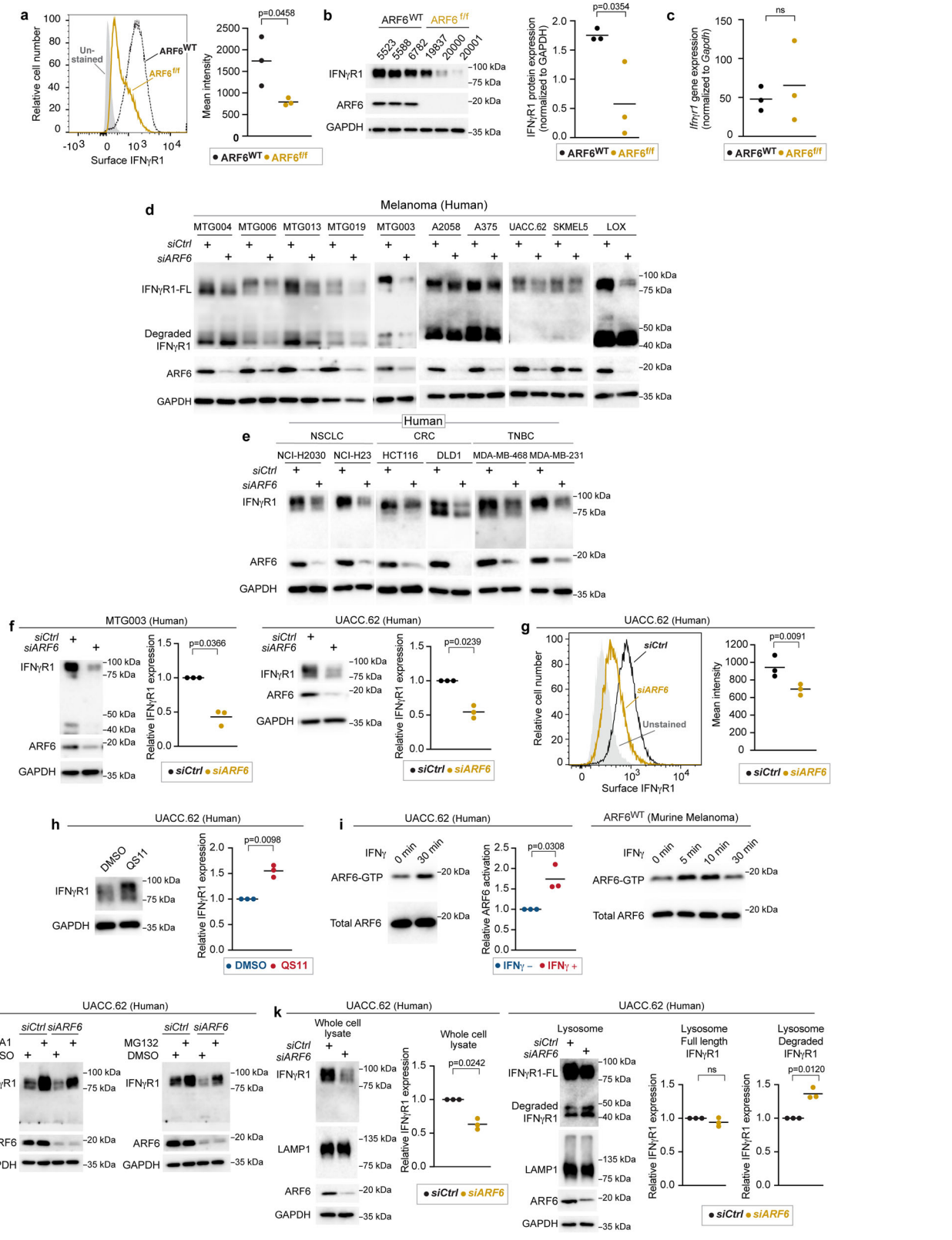

process in malignant cells by demonstrating that ARF6 maintains total and surface levels of the IFNγR1, in the absence of ligand, and that ARF6-dependent regulation of the IFNγR1 protein is a conserved mechanism across high-incidence cancer types (Fig. 6d, e), including NSCLC, CRC, TNBC and melanoma. Thus, ARF6 controls the steady-state availability of IFNγR1 in malignant cells. Future work is needed to understand if ARF6 controls other inflammatory receptors in cancer cells, and how this might contribute to ARF6-mediated remodelling of the TME.

Somatic loss of function mutations and copy number loss of genes in the IFNγ pathway occur in melanomas resistant to ICB[55,56], supporting that tumourintrinsic IFNγ signalling is essential for ICB treatment efficacy. Nevertheless, these somatic events are infrequent and do not fully explain treatment resistance. In addition to cutaneous

https://doi.org/10.1038/s41467-024-50881-1

Fig. 6 | ARF6-dependent IFNγR1 surface expression in murine and human melanoma. a Flow cytometric detection of IFNγR1 cell surface expression in early-passage murine tumour cell lines, $n = 3$ biologically independent tumour cell lines of each genotype. **b** Western blot for IFNγR1 in early-passage murine tumour cell lines, $n = 3$ biologically independent tumour cell lines of each genotype. **c** Quantitative RT-PCR for *Ifngr1* in $n = 3$ biologically independent, early-passage murine tumour cell lines of each genotype. **d**, **e** Western blot for full length (FL) and degraded IFNγR1, ARF6 and GAPDH in human melanoma patient-derived xenograft cells (MTG) and commercially available melanoma lines (**d**), in human non-small cell lung cancer (NSCLC), colorectal cancer (CRC), triple negative breast cancer (TNBC) cell lines (**e**). **f** Quantification of IFNγR1 in MTG003 ($n = 3$ biologically independent experiments) and UACC.62 ($n = 3$ biologically independent experiments) with or without *ARF6* knockdown. **g** Flow cytometric detection of surface expression of IFNγR1 in UACC.62 with or without *ARF6* knockdown, $n = 3$ biologically independent experiments. **h** Western blot for IFNγR1 in UACC.62 without or with 2 μM QS11 treatment for 24 h, $n = 3$ biologically independent experiments. **i** Western blot for total ARF6 and ARF6-GTP in UACC.62 human melanoma cells and murine melanoma cells with or without 500 U/mL IFNγ treatment, $n = 3$ biologically independent experiments. **j** Western blot for indicated proteins in UACC.62 with or without *ARF6* knockdown and with or without 50 nM Bafilomycin A1 or 10 μM MG132 treatment for 6 h. $n = 1$ experiment. **k** Western blot analyses of UACC.62 with or without *ARF6* knockdown as indicated, $n = 3$ biologically independent experiments. **a**–**c**, **g** Two-tailed *t*-test. **f**, **h**, **i**, **k** Two-tailed Ratio paired *t*-test. **a**–**c**, **f**–**h**, **i**, **k** Solid line within data points = mean. See also Supplementary Fig. 6. Source data are provided as a Source Data file.

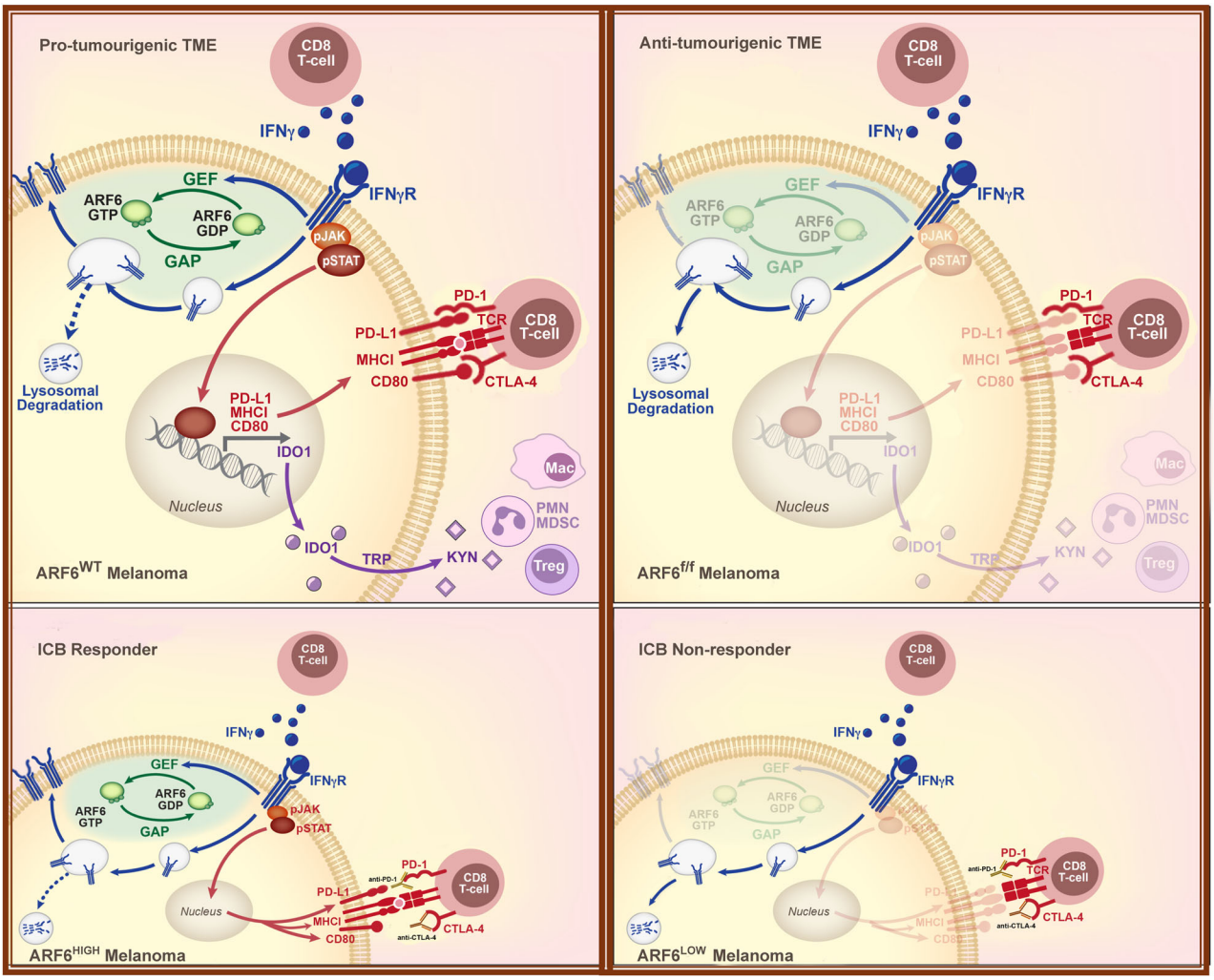

Fig. 7 | Proposed model of ARF6-dependent immune suppression by melanoma. Top panels illustrate an ARF6-dependent mechanism of TME remodelling that accelerates tumour development. ARF6 is activated by IFNγ in a positive feedback loop that diverts the IFNγ receptor away from the lysosome, back to the plasma membrane, augmenting tumourintrinsic, IFNγ-induced expression of checkpoint ligands, PD-L1 and CD80, which inhibit CD8+ T cells that synapse with tumour antigen-loaded MHC-I. ARF6 activation also enhances expression of IFNγ-induced IDO-1, which facilitates recruitment and/or activation of immunosuppressive regulatory T cells (Tregs) and polymorphonuclear-derived myeloid-derived suppressor (PMN-MDSC) cells. Loss of ARF6 diminishes IFNγ-dependent immune suppression, unleashes CD8+ T cell effector function, and restricts tumour development. Bottom panels illustrate the impact of tumour-intrinsic ARF6 on response to immune checkpoint blockade therapy (ICB). Tumours with relatively high ARF6 expression/activation are reliant on IFNγ-driven immune resistance and are vulnerable to ICB. In contrast, tumours with relatively low ARF6 expression/activation progress independent of IFNγ-induced checkpoints and are resistant to therapy.

melanoma, ICB has been approved to treat several types of carcinomas, mesothelioma, a subset of hematopoietic malignancies, and sarcomas[57,58]. Unfortunately, only about 25% of patients with advanced solid tumours treated with ICB respond[37]. Mechanisms that drive low response rates remain incompletely understood. In melanoma, we found that expression of *ARF6*, and the ARF6 GEF *CYTH1* (Supplementary Fig. 4d), are heterogeneous among pre-treatment biopsies from different patients and their expression levels significantly

correlate with response to ICB (Fig. 4b, Supplementary Fig. 4c). Inferior ICB outcomes associated with *ARF6*^{LOW} tumours could be the result of insufficient tumourintrinsic, IFNγ-induced PD-L1, CD80 and MHC-I expression (Figs. 5, and 7, Supplementary Fig. 5b). Moreover, the TME of *ARF6*^{LOW} tumours may be less conducive to ICB. Hence, our work may provide an alternative mechanism to help explain how tumour intrinsic IFNγ signalling could be diminished in ICB-resistant tumours, through downregulation of ARF6.

In this study, the first clue that tumourintrinsic ARF6 controlled the TME came from an unbiased comparison of ARF6^{WT} vs. ARF6^{Q67L} and ARF6$^{f/f}$ primary tumours (Fig. 2a). The decreased expression of inflammatory signatures in bulk transcriptomes from ARF6^{Q67L} primary tumours suggested immune suppression, and this may help explain the enhanced metastatic behaviour in the ARF6^{Q67L} model[24]. Cumulative in vivo data from our immunocompetent models have demonstrated that ARF6 supports distinct, complementary tumour cell functions that can lead to both primary tumour and metastatic progression. While activated ARF6 elicits invasive behaviour through multiple mechanisms[15,16,24,59,60], here we have shown that ARF6 also promotes immune suppression. Thus, our immunocompetent models support that both ARF6-dependent invasion and immune suppression during early tumour formation promote metastatic behaviour (shown previously[24]).

Our study reveals that CD8+ T cells produced more effector molecules (Fig. 3b) in ARF6$^{f/f}$ tumours expressing relatively low MHC-I compared to ARF6^{WT} tumours (Supplementary Fig. 5b). Despite the low tumour MHC-I, more effector CD8+ T cells were detected in ARF6$^{f/f}$ tumours (Fig. 3f) and CD8+ T cells were necessary to limit tumour development in *Arf6*$^{f/f}$ mice (Fig. 3h and Supplementary Fig. 3d). This may be explained by cumulative changes in the ARF6$^{f/f}$ TME that alleviated suppression of CTLs and compensated for the diminished MHC-I, including loss of immune checkpoint ligands PD-L1 and CD80 (Fig. 5), as well as the reduction in Tregs (Fig. 3d) and MDSCs (Fig. 3e). Our data are consistent with findings reported by Benci et al.[61], who described that elimination of tumour IFNγ signalling increased IFNγ produced by CTLs. In this study, CTLs functioned in a supportive role in tumours with low or absent MHC-I expression. Specifically, IFNγ produced by exhausted T cells induced maturation of innate immune cells, including NK cells, to kill tumours. In a more recent study by Lerner et al.[62], MHC-I independent, CTL killing of tumours was revealed. The authors showed that CD8+ T cells maintain the ability to eliminate tumour cells that completely lack MHC-I expression. T cells engaged nonclassical MHC class-I like, NKG2D ligands on tumour cells to release granzyme and perforin. The contribution of these MHC-I independent mechanisms of CTL-dependent tumour elimination, and how they might coordinate in a tumour with variably low MHC-I expression as seen in our model, remains to be investigated.

ARF6-dependent remodelling of the TME and the IFNγR1 trafficking mechanism presented here has potentially broad implications for inflammatory signalling pathways and future development of immuno-therapeutics. In addition to IFNγ (Fig. 6i), ARF6 is activated by and coordinates signalling and functional output of Interleukin-1β[19] and Toll-like receptors[20,21]. Whether ARF6 is critical for trafficking of these, and other inflammatory receptors, remains to be elucidated in both benign and malignant pathologies. Although our data support that ARF6 recycles constitutively internalized IFNγR back to the surface, other ARF6 mechanisms may be at play, including ARF6-dependent intracellular trafficking and subcellular localization of other integral membrane proteins[63] and of mitochondria[64]. Hence, future research into ARF6-dependent basic cellular functions and endocytic transport of immune-modulating cargo may yield important insights that advance the development of immuno-therapeutics.

Methods

Experimental models

Animal studies were performed in accordance with protocol number 00001969, approved by the University of Utah Institutional Animal Care and Use Committee. The *Dct::TVA*; *Braf*^{V600E}; *Cdkn2a*$^{f/f}$ murine model was described previously[24,31]. Creation of the *Arf6*$^{f/f}$ allele was described previously[30]. The *Dct::TVA*; *Braf*^{V600E}; *Cdkn2a*$^{f/f}$; *Arf6*$^{f/f}$ mice were generated by backcrossing the *Arf6*$^{f/f}$ allele into *Dct::TVA*; *Braf*^{V600E}; *Cdkn2a*$^{f/f}$ mice. These *Mus musculus* colonies are on a mixed C57BL/6, FVB, and 129 background and were maintained by random interbreeding. Mice were housed with ad libitum access to food and water on a 12 h light-dark cycle in cages maintained at ~22 °C and 22–30% relative humidity. DF-1 cells infected with RCAS-Cre were suspended in HBSS (Gibco, Cat# 14025-092) and 50 μL of the cell suspension was injected into the flank of neonate mice (0–3 days old) for two consecutive days. Tumour growth was measured by caliper every 1–3 days. Mice were euthanized once the primary tumour measured a maximal size of 2 cm in at least one dimension. Maximal tumour size was not exceeded in this study. Except where stated otherwise, non-tumour bearing mice were followed to 100 days before euthanasia. Tumour volume was calculated as the product of *length* × *width* × *depth* (mm^3). Mice that did not develop tumours were excluded from onset and growth rate calculations. Mice with severely ulcerated tumours and deep tumours were excluded for growth rate calculations due to inaccuracy of size measurements.

Early passage murine tumour cell lines from mice 5523, 5588, 6782, 7657, 21,745, and 21,793 were derived from primary melanomas harvested from *Arf6*^{WT} mice. Cell lines 19,833, 19,835, 19,836, 19,837, 19,840, 19,842, 19,846, 19,957, 19,962, 20,000, 20,001, 20,162, and 20,163 were derived from *Arf6*$^{f/f}$ mice. Briefly, mechanically dissociated tumour cells were cultured with DMEM/F12 (ThermoFisher Scientific, Cat# 11330-032) supplemented with 10% v/v FBS (Atlas Biologicals, Cat# F-0500-DR), 0.5% v/v gentamicin (ThermoFisher Scientific, Cat# 15710072), 1% MEM Non-Essential Amino Acids Solution (ThermoFisher Scientific, Cat# 11140050) under standard conditions at 37 °C in a humidified atmosphere with 5% CO_2.

Human melanoma cell lines, A375, LOX-IMVI, SK-MEL-5, and UACC.62, were provided by Dr. M. VanBrocklin, Huntsman Cancer Institute (HCI). A2058 cells were purchased from the ATCC (Cat# CRL11147D). Early passage patient-derived human melanoma cell lines MTG003, MTG004, MTG006, MTG013, and MTG019, were provided by the Preclinical Research Resource (PRR) at HCI. A2058 and A375 cells were maintained in DMEM-high glucose (ThermoFisher Scientific, Cat# 11995073) supplemented with 10% v/v FBS, 1% v/v penicillin-streptomycin-glutamine. LOX-IMVI, SK-MEL-5, and UACC.62 cells were maintained in RPMI1640-high glucose media (ThermoFisher Scientific, Cat# A1049101) supplemented with 10% v/v FBS, 1% v/v penicillin-streptomycin-glutamine. Patient-derived human melanoma cell lines were maintained in Mel2 media provided by the PRR. Cells were incubated at 37 °C in a humidified atmosphere with 5% CO_2.

Non-small cell lung cancer cell lines, NCI-H2030, NCI-H23, were purchased from ATCC (Cat# CRL-5914 and CRL-5800) and maintained in RPMI1640-high glucose media supplemented with 10% v/v FBS, and 1% v/v penicillin-streptomycin-glutamine. Colorectal carcinoma cell line, HCT116, was purchased from ATCC (Cat# CCL-247). Colorectal carcinoma cell line, DLD-1, was provided by the PRR. HCT116 cells were maintained in McCoy's 5A Modified media supplemented with 10% v/v FBS, and 1% v/v penicillin-streptomycin-glutamine. DLD-1 cells were maintained in RPMI1640-high glucose media supplemented with 10% v/v FBS, and 1% v/v penicillin-streptomycin-glutamine. Breast adenocarcinoma cell line, MDA-MB-468, was provided by the PRR. Breast adenocarcinoma cell line, MDA-MB-231, was purchased from ATCC (Cat# HTB-26). MDA-MB-468 and MDA-MB-231 cells were maintained

in Leibovitz's L-15 media supplemented with 10% v/v FBS, and 1% v/v penicillin-streptomycin-glutamine. Cells were incubated at 37 °C in a humidified atmosphere with 5% CO_2.

Human cell line authentication was performed with STR profiling at the University of Utah Genomics core facility using the Promega (Madison, WI) GenePrint 10 system.

DF-1 and A375-TVA cells were provided by S. Holmen (HCI). DF-1 cells were maintained in DMEM-high glucose supplemented with 10% FBS, 0.5% v/v gentamicin, and maintained at 39 °C, with 5% CO_2. A375-TVA cells were maintained in DMEM-high glucose supplemented with 10% FBS, 0.5% v/v gentamicin, at 37 °C with 5% CO_2 and were used to verify RCAS/Cre expression in DF-1 cells.

RNA interference

Silencing of endogenous genes in human cell lines was performed by sequential transfection of siRNA (*ARF6*, Qiagen Cat# 1027417; GeneGlobe S02757286), (*CYTH1*, Qiagen, Cat# 1027416), and compared to AllStars Negative Control siRNA (Qiagen, Cat# 1027181) at a final concentration of 40 nM using Lipofectamine™ RNAiMAX transfection reagent (ThermoFisher Scientific, Cat# 13778150). Briefly, cells were seeded in a 6-well plate and first transfected with 40 nM siRNA mixed with 7.5 μL of Lipofectamine™ RNAiMAX transfection reagent. After 24 h, transfections were repeated under the same conditions. Cells were collected 24 h after the second transfection for flow cytometry and western blot analyses.

Histology

Mouse tissues were fixed in 10% neutral buffered formalin overnight then placed in 70% ethyl alcohol before paraffin-embedding (FFPE). Four-micron sections of primary murine tumours were assessed by a board-certified pathologist (A.H.G.) blinded to the genetic identity of each sample for evaluation of PD-L1 immunohistochemical staining and for evaluation of tumour-infiltrating lymphocyte clusters.

Flow cytometry analysis

When the tumours reached 2 cm in greatest dimension, both the tumours and spleens were harvested after euthanasia. Portions of the tumours and the whole spleen were then taken, and their weights were recorded for flow cytometry analysis. Tumours were minced into small fragments and incubated with GentleMACS C tubes (Miltenyi Biotec, Cat# 130-093-237) with a serum free-DMEM/F12 solution containing digestive enzymes from a Mouse Tumour Dissociation Kit (Miltenyi Biotech, Cat# 130-096-730). Tumours were disaggregated into single-cell suspensions using a Miltenyi GentleMACS Octo Dissociator (Miltenyi Biotec). Tumour cells were filtered through a 70 μm nylon filter and treated with an RBC lysis solution (ThermoFisher Scientific, Cat# 00-4300-54). Spleens were disaggregated into single-cell suspensions by mechanical disruption and filtered through a 40 μm nylon filter and treated with an RBC lysis solution. 3Holmen 4×10^6 cells from tumour or spleen were stained with antibodies against cell surface antigens for 1 h on ice before flow cytometry analysis (BD Fortessa). For intracellular staining, cells were fixed and permeablized with a fixation/permeablization reagent (ThermoFisher Scientific, Cat# 00-5523-00) according to the manufacturer's instructions. Cells were stained with antibodies against intracellular antigens for 30 min on ice before flow cytometry analysis. Cell lines were disaggregated into single-cell suspensions using a Miltenyi GentleMACS Octo Dissociator (Miltenyi Biotec). Staining was performed according to the manufacturer's instructions.

To assess IFNγ and granzyme B (GzmB) production, tumours and spleens were disaggregated into single-cell suspensions using the method described above. 1×10^6 cells were seeded and added to a cell activation cocktail (BioLegend, Cat# 423303) and incubated at 37 °C in a 5% CO_2 incubator for 6 h. Stimulated cells were collected and stained with antibodies against cell surface antigens. After fixation and permeabilization, cells were stained with antibodies for intracellular IFNγ or GzmB for 30 min on ice before flow cytometry analysis. Antibodies used for flow cytometry analysis are listed in Supplementary Table 4. Gating strategies for flow cytometry analyses are shown in Supplementary Fig. 3a and in Supplementary Fig. 7. Further information on gene expression markers for distinguishing immune cell lineages is shown in Supplementary Table 5. The absolute numbers of CD45+ cells per gram of tumour (Supplementary Fig. 2a) were determined by beads (Spherotech, Cat#: ACFP-100-3) using flow cytometry according to the manufacturer's instructions.

Quantitative reverse transcription polymerase chain reaction (qRT-PCR)

Total RNA from six independent primary murine tumour cell lines, 3 $ARF6^{WT}$ (5523, 5588, and 6782) and 3 $ARF6^{f/f}$ (19837, 20000, and 20001), were treated for 8 h with 500 U/ml murine IFNγ then collected in RNAlater (ThermoFisher Scientific, Cat# AM7024). RNA was extracted using an RNeasy Plus kit (Qiagen, Cat# 74034) according to the manufacturer's instructions. Extracted RNAs from each sample were converted into cDNA using SuperScript IV VILO (SSIV VILO) Master Mix (ThermoFisher Scientific, Cat# 11756050). QRT-PCR was performed in triplicate for each sample using PowerUp™ SYBR™ Green Master Mix (ThermoFisher Scientific, Cat# A25780) and run using a QuantStudio™ 6 Flex Real-Time PCR System (ThermoFisher Scientific) on 96-well plates. Primers used for qRT-PCR are shown in Supplementary Table 4. The specificity of the amplicons was assessed by melting curve analyses. Relative mRNA expression of each gene was calculated using the number of cycles needed to reach the specific threshold of detection (CT) and normalized to the expression of *Gapdh*.

Western blot and ARF6-GTP-pulldown

Cells were lysed using Pierce® IP Lysis buffer (ThermoFisher Scientific, Cat # 87788) with 1X Halt™ Protease and Phosphatase Inhibitor Cocktail (ThermoFisher Scientific, Cat# 78442). Protein concentrations were determined using the Pierce™ BCA Protein Assay Kit (ThermoFisher Scientific, Cat# 23227). Cell lysates were boiled with SDS sample buffer. Proteins from the cell lysates were separated by SDS polyacrylamide gel electrophoresis (SDS–PAGE) and transferred to polyvinylidene difluoride (PVDF) membranes (ThermoFisher Scientific, Cat# 88518). The PVDF membranes were blocked with TBST (10 mM Tris-HCl, 150 mM NaCl and 0.1% v/v Tween-20) containing 5% v/v skim milk and incubated with primary antibodies. After washing in TBST, membranes were incubated with HRP-conjugated secondary antibodies then washed with TBST before developing with Western Lightning™ Plus Chemiluminescence Reagent (PerkinElmer, Cat# NEL103001EA) or SuperSignal™ West Dura Extended Duration Substrate (ThermoFisher Scientific, Cat# 37075). Luminescent signal was detected using the Azure c300 or c600 (Azure Biosystems). ImageJ (NIH, Bethesda, MD, USA) was used to quantify the intensity of bands on the blots. Images were adjusted equally for brightness and contrast using ImageJ or Adobe Photoshop (Adobe Inc.). Antibodies used for western blots are listed in Supplementary Table 4.

ARF6-GTP pull-downs were performed using GGA3 PBD Agarose beads (Cell Biolabs, STA-419) as previously described[22]. Briefly, cells were starved in 0.1% FBS for 16 h before treatment IFNγ or cells were treated with QS11 or transfected with pcDNA3.1-ACAP1-C-(K)DYK (GenScript Cat#: OHu32019D) and empty vector (GenScript Cat#: SC2092) using Lipofectamine™ 3000 Transfection Reagent (Thermo Scientific Cat#: L3000008). After treatment, cells were lysed with pulldown lysis buffer (Cell Biolabs, Cat# 240102) including 1X Halt™ Protease and Phosphatase Inhibitor Cocktail. Lysates were centrifuged, and supernatants were added to GGA3-conjugated beads and agitated for 1 h at 4 °C. Beads were washed in ARF6-pulldown lysis buffer and prepared for western blot analysis.

IFNγR1 internalization assay

Cell-surface proteins were labelled with EZ-Link Sulfo-NHS-SS-Biotin (ThermoFisher Scientific cat# 21331) at 0.8 mg/mL in PBS at 4 °C for 30 min. Excess biotin was removed by washing the cells with ice-cold 20 mM glycine in PBS. Cells were then incubated at 37 °C in warm media for 30 min to allow internalization of biotinylated surface proteins. The remaining cell-surface biotin was cleaved by washing with GSH buffer (50 mM glutathione, 75 mM NaOH, 75 mM NaCl, 10 mM EDTA, 0.1%BSA, pH 7–7.5) twice for 15 min at 4 °C. GSH was then quenched by washing with 5 mg/mL ice-cold iodoacetamide in PBS. Cells were then washed with ice-cold PBS and lysed on ice using Pierce® IP Lysis buffer with 1x HALT Protease and Phosphatase Inhibitor Cocktail. Lysates were then incubated with High-Capacity Streptavidin Agarose Resin (ThermoFisher Scientific cat# 20357) at 4 °C for 60 min. Resin beads were then washed with Pierce® IP Lysis buffer. Internalized IFNγR1 was detected by Western blot.

IFNγR1 recycling assay

Cell-surface proteins were labelled with EZ-Link Sulfo-NHS-SS-Biotin for 30 min. Cells were then incubated at 37 °C in warm media for 60 min to allow internalization of biotinylated surface proteins. The remaining cell-surface biotin was cleaved by GSH buffer. Cells were reincubated at 37 °C media for indicated times with DMSO or ARF6 inhibitor SecinH3 (30 μM) for IFNγR1 recycling. After recycling, the recycled cell-surface biotin was removed by GSH buffer and cells were lysed followed with streptavidin-biotin pulldown. Remained cytosolic IFNγR1 was detected by Western blot.

Arf6 mRNA in situ hybridization

Arf6 mRNA was detected in four μm tissue sections using a custom *Arf6* probe (Cat# 1205481-C1, Advanced Cell Diagnostics), targeting a sequence located between the loxP sites of the $Arf6^{f/f}$ allele, and the RNAscope 2.5 HD Reagent Kit−RED (Cat# 3222350, Advanced Cell Diagnostics) according to the manufacturer's instructions.

Lysosome enrichment

RNA interference was performed on UACC.62 cells as described above. Lysosome enrichment was performed using a Lysosome Enrichment Kit (ThermoFisher Scientific, Cat# 89839) according to the manufacturer's instructions. Briefly, cells were disrupted in the supplied lysis buffers using a Dounce homogenizer. Following centrifugation to pellet debris, supernatants were loaded on 15–30% Optiprep (Millipore-Sigma, Cat# D1556) step gradients and centrifuged at 145,000 × *g* for 2 h. The lysosome-enriched fractions were collected and pelleted prior to lysis and quantitation for use in western blot analysis.

In vivo CD8+ T-cell depletion

At 5 weeks post DF1 RCAS-Cre injection, mice were treated with antibodies prior to tumour onset. Anti-CD8 (200 μg/mouse, Bio X Cell, Cat# BE0117) or rat IgG2b isotype control (200 μg/mouse, Bio X Cell, Cat# BE0090) antibodies were injected intraperitoneally twice per week for 8 weeks or until the tumour measured 2 cm in one dimension. CD8+ cell depletion was verified by flow cytometry.

In vivo anti-PD-1 treatment

Anti-PD-1 treatment was initiated prior to palpable tumour onset, when microscopic disease was expected, in $Arf6^{WT}$ mice at 5 weeks, and in $Arf6^{f/f}$ mice at 7 weeks. Anti-PD-1 (8 mg/kg, Bio X Cell, Cat# BE0146) was administered intraperitoneally twice per week for 5 weeks or <5 weeks if the tumour reached 2 cm in greatest dimension. A second cohort of $Arf6^{WT}$ and $Arf6^{f/f}$ mice containing established tumours was treated with anti-PD-1 when tumours measured ~0.4–0.5 cm in greatest dimension. Anti-PD-1 was administered at 8 mg/kg and mice were euthanized once the primary tumour measured 2 cm in one dimension.

Proteomics

Protein extraction and reverse-phase protein array of frozen mouse tumours was performed by the MD Anderson Cancer Center Functional Proteomic RPPA Core Facility.

Single-cell RNA sequencing and analysis

Tumours (2 cm in greatest dimension) were dissociated as described above under flow cytometry analysis. Resulting cells from tumours were stained with antibodies against CD45 and sorted (FACSAria 5 Laser). CD45+ cells were then subjected to single-cell RNA sequencing (scRNAseq) analysis using the 10X Genomics Chromium system and run on an Illumina NovaSeq instrument by the High Throughput Genomics core (University of Utah).

The Fastq files were aligned to the mm10 mouse reference from 10X genomics (refdata-gex-mm10-2020-A) using cellranger count (version 6.0.1) to create quality control metrics, Loupe Browser files, and filtered gene barcode matrices[65]. The filtered gene barcode matrices were loaded into the Seurat 4.1.1 package and merged into a single matrix[66]. About 5% of cells with more than 20% mitochondrial reads, fewer than 200 features, or more than 8000 features were removed and counts were normalized using the sctransform method[67]. Twenty dimensions and 0.8 resolution were selected for clustering and the non-linear dimensional reduction with UMAP. Cluster markers and differentially expressed genes (DEGs) were identified using the Wilcoxon Rank Sum test in Seurat. The list of cluster markers and significant genes were analyzed using the Enrichr website to identify over-represented gene sets, pathways and cell types using a Fisher's Exact Test[68]. Cell type labels were assigned to cells using a nearest neighbour classifier in the SingleR package[69]. T cell clusters were then projected onto a T cell reference using the ProjecTILs package[70]. See Supplementary Information for a detailed list of gene expression markers used for manual annotation of immune cell lineages.

Macrophage single-cell RNA sequencing analysis was performed using the R package Seurat (version 4)[71]. Low-quality cells (greater than 10% mitochondrial genes, fewer than 1000 or more than 5000 RNA features per cell) and lymphocytes (*Ighm* > 0.001 and *Cd3e* > 0.001) were filtered out. Gene expression values were normalized, scaled, and aligned across conditions. Then, cells were clustered and UMAP was used to visualize the distribution of these clusters. A cluster of cells enriched with *Ly6c1*, *Gpihbp1*, *Cd36*, and *podxl* genes, with extremely low frequencies (0.15% and 0.04% in $ARF6^{WT}$ and $ARF6^{f/f}$ tumours, respectively) of *Cd3e/Ighm* negative cells, were excluded from the UMAP. DEGs for selected clusters were obtained using the Seurat function FindMarkers with the default parameters (non-parametric Wilcoxon rank sum test). To facilitate the exploration of genes of interest, the default logFC threshold was reduced, enabling the discovery of several smaller, yet significant, changes in gene expression that had been previously excluded.

Bulk RNA sequencing and analysis

RNA was extracted from fresh-frozen mouse tumours using Direct-zol RNA Miniprep Plus Kit (Zymogenetics) after frozen section histologic confirmation of high tumour content. RNA-sequencing was performed on 6 tumours from each genotype ($Arf6^{WT}$, $Arf6^{f/f}$, and $Arf6^{Q67L}$) using Illumina TruSeq Stranded mRNA Library Preparation Kit with polyA selection followed by Illumina HiSeq 2500 125-cycle paired-end sequencing.

Bulk tumour RNA sequencing analysis included GSEA using MSigDB Hallmark (NES scores). The mouse GRCm38 genome and gene feature files were downloaded from Ensembl (release 90) and a reference database was created using STAR (version 2.5.2b) with splice junctions optimized for 125 base pair reads[72]. Reads were trimmed of adaptors using cutadapt (version 1.16)[73] and aligned to the reference database using STAR in two-pass mode to output a BAM file sorted by coordinates. Mapped reads were assigned to annotated genes using

featureCounts (version 1.6.3)[74]. The output files from cutadapt, FastQC, FastQ Screen, Picard CollectRnaSeqMetrics, STAR, and featureCounts were summarized using MultiQC to check for any sample outliers[75]. DEGs were identified using a 10% false discovery rate with DESeq2 (version 1.26.0)[76]. Significantly enriched Hallmark, KEGG, and REACTOME pathways from MSigDB were detected using the fast gene set enrichment package[77].

Analysis of Leeds Melanoma Cohort

The normalized Leeds Melanoma Cohort gene expression dataset (EGAD00010001561) was downloaded from the European Genome-Phenome Archive with permission from the University of Leeds, United Kingdom. The first seven columns in the "LMCFFPEmelanomanormalised.txt" file were used to create a survival table with stage, status, and overall survival time. The remaining columns included Illumina HT12.4 probes that were mapped to gene names using the illuminaHumanv4.db BioConductor package[78]. The log2 normalized counts from 40 ARF6-related genes were analyzed using a proportional hazards regression model using the coxph function in the survival package in R (version 3.5-5)[79]. In addition, gene expression within each AJCC stage class 1, 2, and 3 was modelled separately. Survival curves were plotted using high and low-expression groups divided into both medians and quartiles.

Cancer-Immu analysis

A pan-cancer analysis was performed on pre-treatment biopsy datasets using all samples from all thirteen melanoma study cohorts included in the Cancer-Immu Immunogenomic Atlas for ICB Immunotherapy[39]. Individual genes from the ARF6 pathway (Supplementary Table 2), were queried with default parameters (median gene expression, sum cutoff of 0.5) with the Pan-cancer analysis, Transcriptomic: Expression tool for single genes, and the Transcriptomic: Expression sum tool for multiple genes.

TCGA analysis

TCGA melanoma RNA-Seq data were extracted from all melanoma TCGA RNA-Seq data (GDC Data Release 34.0 queried on July 27, 2022, in the TCGA_SKCM_v34.html). Survival times were generated using days to death and days to last follow-up data. Samples without survival data were excluded. Each gene was evaluated individually. Samples were stratified into *ARF6* or *CYTH1* high vs. low groups by median centring of expression levels for each gene. Survival p values were calculated by log-rank (Mantel-Cox) test.

Quantification and statistical analysis

Statistical tests were assessed using Prism 8 or 9 software (GraphPad) or SAS version 9.4 (SAS Institute Inc). Quantitative values are represented as the mean of at least three replicates.

Reporting summary

Further information on research design is available in the Nature Portfolio Reporting Summary linked to this article.

Data availability

The raw and processed single-cell and bulk RNA sequence data from murine tumours generated in this study have been deposited in the Gene Expression Omnibus (GEO) database under accession code GSE253094. The publicly released data used in this study are available in the GEO database under accession code GSE129392. The Leeds Melanoma Cohort gene expression dataset is available under restricted access at the EGA under accession number EGAD00010001561. Data access can be granted via the EGA with completion of a data access agreement. The TCGA publicly available data used in this study are available in the Genomic Data Commons database under accession code TCGA-SKCM. Human datasets can be analyzed through Cancer-Immu: https://bioinfo.vanderbilt.edu/database/Cancer-Immu/. The remaining data are available within the Article, Supplementary Information or Source Data file. Source data are provided with this paper.

References

1. Hanahan, D. Hallmarks of cancer: new dimensions. *Cancer Discov.* **12**, 31–46 (2022).
2. Wellenstein, M. D. & de Visser, K. E. Cancer-cell-intrinsic mechanisms shaping the tumor immune landscape. *Immunity* **48**, 399–416 (2018).
3. Ghorani, E., Swanton, C. & Quezada, S. A. Cancer cell-intrinsic mechanisms driving acquired immune tolerance. *Immunity* **56**, 2270–2295 (2023).
4. Bejarano, L., Jordao, M. J. C. & Joyce, J. A. Therapeutic targeting of the tumor microenvironment. *Cancer Discov.* **11**, 933–959 (2021).
5. Nirmal, A. J. et al. The spatial landscape of progression and immunoediting in primary melanoma at single-cell resolution. *Cancer Discov.* **12**, 1518–1541 (2022).
6. Thomas, N. E. et al. Tumor-infiltrating lymphocyte grade in primary melanomas is independently associated with melanoma-specific survival in the population-based genes, environment and melanoma study. *J. Clin. Oncol. Off. J. Am. Soc. Clin. Oncol.* **31**, 4252–4259 (2013).
7. Wong, S. L. et al. Sentinel lymph node biopsy for melanoma: American Society of Clinical Oncology and Society of Surgical Oncology joint clinical practice guideline. *J. Clin. Oncol. Off. J. Am. Soc. Clin. Oncol.* **30**, 2912–2918 (2012).
8. McKenzie, B. & Valitutti, S. Resisting T cell attack: tumor-cell-intrinsic defense and reparation mechanisms. *Trends Cancer* **9**, P198–211 (2022).
9. Cullen, P. J. & Steinberg, F. To degrade or not to degrade: mechanisms and significance of endocytic recycling. *Nat. Rev. Mol. cell Biol.* **19**, 679–696 (2018).
10. D'Souza-Schorey, C. et al. ARF6 targets recycling vesicles to the plasma membrane: insights from an ultrastructural investigation. *J. Cell Biol.* **140**, 603–616 (1998).
11. Schweitzer, J. K., Sedgwick, A. E., & D'Souza-Schorey, C. ARF6-mediated endocytic recycling impacts cell movement, cell division and lipid homeostasis. *Semin. Cell Dev. Biol.* **22**, 39–47 (2011).
12. Prigent, M. et al. ARF6 controls post-endocytic recycling through its downstream exocyst complex effector. *J. Cell Biol.* **163**, 1111–1121 (2003).
13. Cavenagh, M. M. et al. Intracellular distribution of Arf proteins in mammalian cells. Arf6 is uniquely localized to the plasma membrane. *J. Biol. Chem.* **271**, 21767–21774 (1996).
14. Grossmann, A. H. et al. The small GTPase ARF6 regulates protein trafficking to control cellular function during development and in disease. *Small GTPases* **10**, 1–12 (2016).
15. Grossmann, A. H. et al. The small GTPase ARF6 stimulates beta-catenin transcriptional activity during WNT5A-mediated melanoma invasion and metastasis. *Sci. Signal.* **6**, ra14 (2013).
16. Tague, S. E. & Muralidharan, V. & D'Souza-Schorey, C. ADP-ribosylation factor 6 regulates tumor cell invasion through the activation of the MEK/ERK signaling pathway. *Proc. Natl Acad. Sci. USA* **101**, 9671–9676 (2004).
17. Pellon-Cardenas, O., Clancy, J. & Uwimpuhwe, H. & D'Souza-Schorey, C. ARF6-regulated endocytosis of growth factor receptors links cadherin-based adhesion to canonical Wnt signaling in epithelia. *Mol. Cell. Biol.* **33**, 2963–2975 (2013).
18. Morishige, M. et al. GEP100 links epidermal growth factor receptor signalling to Arf6 activation to induce breast cancer invasion. *Nat. Cell Biol.* **10**, 85–92 (2008).
19. Zhu, W. et al. Interleukin receptor activates a MYD88-ARNO-ARF6 cascade to disrupt vascular stability. *Nature* **492**, 252–255 (2012).

20. Davis, C. T. et al. ARF6 inhibition stabilizes the vasculature and enhances survival during endotoxic shock. *J. Immunol.* **192**, 6045–6052 (2014).
21. Wu, J. Y. & Kuo, C. C. TLR9-mediated ARF6 activation is involved in advancing CpG ODN cellular uptake. *Commun. Integr. Biol.* **5**, 316–318 (2012).
22. Yoo, J. H. et al. ARF6 is an actionable node that orchestrates oncogenic GNAQ signaling in uveal melanoma. *Cancer Cell* **29**, 889–904 (2016).
23. Hashimoto, S. et al. ARF6 and AMAP1 are major targets of KRAS and TP53 mutations to promote invasion, PD-L1 dynamics, and immune evasion of pancreatic cancer. *Proc. Natl Acad. Sci. USA* **116**, 17450–17459 (2019).
24. Yoo, J. H. et al. The small GTPase ARF6 activates PI3K in melanoma to induce a prometastatic state. *Cancer Res.* **79**, 2892–2908 (2019).
25. Nsengimana, J. et al. β-Catenin-mediated immune evasion pathway frequently operates in primary cutaneous melanomas. *J. Clin. Investig.* **128**, 2048–2063 (2018).
26. Jackson, T. R. et al. ACAPs are arf6 GTPase-activating proteins that function in the cell periphery. *J. Cell Biol.* **151**, 627–638 (2000).
27. Ma, Z., Nie, Z., Luo, R., Casanova, J. E. & Ravichandran, K. S. Regulation of Arf6 and ACAP1 signaling by the PTB-domain-containing adaptor protein GULP. *Curr. Biol.* **17**, 722–727 (2007).
28. Xu, R. et al. A Rab10-ACAP1-Arf6 GTPases cascade modulates M4 muscarinic acetylcholine receptor trafficking and signaling. *Cell Mol. Life Sci.* **80**, 87 (2023).
29. Ismail, S. A., Vetter, I. R., Sot, B. & Wittinghofer, A. The structure of an Arf-ArfGAP complex reveals a Ca2+ regulatory mechanism. *Cell* **141**, 812–821 (2010).
30. Zhu, W. et al. Small GTPase ARF6 controls VEGFR2 trafficking and signaling in diabetic retinopathy. *J. Clin. Investig.* **127**, 4569–4582 (2017).
31. Cho, J. H. et al. AKT1 activation promotes development of melanoma metastases. *Cell Rep.* **13**, 898–905 (2015).
32. Donaldson, J. G. & Jackson, C. L. ARF family G proteins and their regulators: roles in membrane transport, development and disease. *Nat. Rev. Mol. Cell Biol.* **12**, 362–375 (2011).
33. Sumiyoshi, M. et al. Arf1 and Arf6 synergistically maintain survival of T cells during activation. *J. Immunol.* **206**, 366–375 (2021).
34. Singh, P., Ravanan, P. & Talwar, P. Death associated protein kinase 1 (DAPK1): a regulator of apoptosis and autophagy. *Front Mol. Neurosci.* **9**, 46 (2016).
35. Veglia, F., Sanseviero, E. & Gabrilovich, D. I. Myeloid-derived suppressor cells in the era of increasing myeloid cell diversity. *Nat. Rev. Immunol.* **21**, 485–498 (2021).
36. Ribas, A. Adaptive immune resistance: how cancer protects from immune attack. *Cancer Discov.* **5**, 915–919 (2015).
37. Kim, T. K., Vandsemb, E. N., Herbst, R. S. & Chen, L. Adaptive immune resistance at the tumour site: mechanisms and therapeutic opportunities. *Nat. Rev. Drug Discov.* **21**, 529–540 (2022).
38. Gocher, A. M., Workman, C. J. & Vignali, D. A. A. Interferon-γ: teammate or opponent in the tumour microenvironment? *Nat. Rev. Immunol.* **22**, 158–172 (2022).
39. Yang, J. et al. A pan-cancer immunogenomic atlas for immune checkpoint blockade immunotherapy. *Cancer Res.* **82**, 539–542 (2021).
40. Sztul, E. et al. ARF GTPases and their GEFs and GAPs: concepts and challenges. *Mol. Biol. cell* **30**, 1249–1271 (2019).
41. Ogasawara, M. et al. Similarities in function and gene structure of cytohesin-4 and cytohesin-1, guanine nucleotide-exchange proteins for ADP-ribosylation factors. *J. Biol. Chem.* **275**, 3221–3230 (2000).
42. Melanoma: Cutaneous, <nccn.org> (2023).
43. The Cancer Genome Atlas Network. Genomic classification of cutaneous melanoma. *Cell* **161**, 1681–1696 (2015).
44. Lee, S. J. et al. Interferon regulatory factor-1 is prerequisite to the constitutive expression and IFN-gamma-induced upregulation of B7-H1 (CD274). *FEBS Lett.* **580**, 755–762 (2006).
45. Mezrich, J. D. et al. An interaction between kynurenine and the aryl hydrocarbon receptor can generate regulatory T cells. *J. Immunol.* **185**, 3190–3198 (2010).
46. Holmgaard, R. B. et al. Tumor-expressed IDO recruits and activates MDSCs in a treg-dependent manner. *Cell Rep.* **13**, 412–424 (2015).
47. Nistico, P. et al. Effect of recombinant human leukocyte, fibroblast, and immune interferons on expression of class I and II major histocompatibility complex and invariant chain in early passage human melanoma cells. *Cancer Res.* **50**, 7422–7429 (1990).
48. Giacomini, P. et al. Regulation of the antigenic phenotype of human melanoma cells by recombinant interferons. *Anticancer Res* **6**, 877–884 (1986).
49. Zhang, Q. et al. Small-molecule synergist of the Wnt/β-catenin signaling pathway. *Proc. Natl Acad. Sci. USA* **104**, 7444–7448 (2007).
50. Chabu, C., Li, D. M. & Xu, T. EGFR/ARF6 regulation of Hh signalling stimulates oncogenic Ras tumour overgrowth. *Nat. Commun.* **8**, 14688 (2017).
51. Menju, T. et al. Engagement of overexpressed Her2 with GEP100 induces autonomous invasive activities and provides a biomarker for metastases of lung adenocarcinoma. *PloS one* **6**, e25301 (2011).
52. Palacios, F., Price, L., Schweitzer, J., Collard, J. G., & D'Souza-Schorey, C. An essential role for ARF6-regulated membrane traffic in adherens junction turnover and epithelial cell migration. *EMBO J.* **20**, 4973–4986 (2001).
53. Hu, B. et al. ADP-ribosylation factor 6 regulates glioma cell invasion through the IQ-domain GTPase-activating protein 1-Rac1-mediated pathway. *Cancer Res.* **69**, 794–801 (2009).
54. Celada, A. & Schreiber, R. D. Internalization and degradation of receptor-bound interferon-gamma by murine macrophages. Demonstration of receptor recycling. *J. Immunol.* **139**, 147–153 (1987).
55. Zaretsky, J. M. et al. Mutations associated with acquired resistance to PD-1 blockade in melanoma. *N. Engl. J. Med.* **375**, 819–829 (2016).
56. Gao, J. et al. Loss of IFN-gamma pathway genes in tumor cells as a mechanism of resistance to Anti-CTLA-4 therapy. *Cell* **167**, 397–404.e399 (2016).
57. Korman, A. J., Garrett-Thomson, S. C. & Lonberg, N. The foundations of immune checkpoint blockade and the ipilimumab approval decennial. *Nat. Rev. Drug Discov.* **21**, 509–528 (2022).
58. Saerens, M. et al. Immune checkpoint inhibitors in treatment of soft-tissue sarcoma: a systematic review and meta-analysis. *Eur. J. Cancer* **152**, 165–182 (2021).
59. Muralidharan-Chari, V. et al. ADP-ribosylation factor 6 regulates tumorigenic and invasive properties in vivo. *Cancer Res.* **69**, 2201–2209 (2009).
60. Muralidharan-Chari, V. et al. ARF6-regulated shedding of tumor cell-derived plasma membrane microvesicles. *Curr. Biol.* **19**, 1875–1885 (2009).
61. Benci, J. L. et al. Opposing functions of interferon coordinate adaptive and innate immune responses to cancer immune checkpoint blockade. *Cell* **178**, 933–948.e914 (2019).
62. Lerner, E. C. et al. CD8(+) T cells maintain killing of MHC-I-negative tumor cells through the NKG2D-NKG2DL axis. *Nat. Cancer* **4**, 1258–1272 (2023).
63. Montagnac, G. et al. Decoupling of activation and effector binding underlies ARF6 priming of fast endocytic recycling. *Curr. Biol.* **21**, 574–579 (2011).
64. Onodera, Y., Nam, J. M., Horikawa, M., Shirato, H. & Sabe, H. Arf6-driven cell invasion is intrinsically linked to TRAK1-mediated mitochondrial anterograde trafficking to avoid oxidative catastrophe. *Nat. Commun.* **9**, 2682 (2018).

65. Zheng, G. X. et al. Massively parallel digital transcriptional profiling of single cells. *Nat. Commun.* **8**, 14049 (2017).
66. Satija, R., Farrell, J. A., Gennert, D., Schier, A. F. & Regev, A. Spatial reconstruction of single-cell gene expression data. *Nat. Biotechnol.* **33**, 495–502 (2015).
67. Hafemeister, C. & Satija, R. Normalization and variance stabilization of single-cell RNA-seq data using regularized negative binomial regression. *Genome Biol.* **20**, 296 (2019).
68. Chen, E. Y. et al. Enrichr: interactive and collaborative HTML5 gene list enrichment analysis tool. *BMC Bioinforma.* **14**, 128 (2013).
69. Aran, D. et al. Reference-based analysis of lung single-cell sequencing reveals a transitional profibrotic macrophage. *Nat. Immunol.* **20**, 163–172 (2019).
70. Andreatta, M. et al. Interpretation of T cell states from single-cell transcriptomics data using reference atlases. *Nat. Commun.* **12**, 2965 (2021).
71. Hao, Y. et al. Integrated analysis of multimodal single-cell data. *Cell* **184**, 3573–3587.e3529 (2021).
72. Dobin, A. et al. STAR: ultrafast universal RNA-seq aligner. *Bioinformatics* **29**, 15–21 (2013).
73. Martin, M. Cutadapt removes adapter sequences from high-throughput sequencing reads. *EMBnet. J.* **17**, 10–12 (2011).
74. Liao, Y., Smyth, G. K. & Shi, W. featureCounts: an efficient general purpose program for assigning sequence reads to genomic features. *Bioinformatics* **30**, 923–930 (2014).
75. Ewels, P., Magnusson, M., Lundin, S. & Kaller, M. MultiQC: summarize analysis results for multiple tools and samples in a single report. *Bioinformatics* **32**, 3047–3048 (2016).
76. Love, M. I., Huber, W. & Anders, S. Moderated estimation of fold change and dispersion for RNA-seq data with DESeq2. *Genome Biol.* **15**, 550 (2014).
77. Korotkevich, G. et al. Fast gene set enrichment analysis. Bioconductor Open Source Software for Bioinformatics https://doi.org/10.18129/B9.bioc.fgsea (2021).
78. Dunning, M., Lynch, A., Eldridge, M. Illumina HumanHT12v4 annotation data (chip illuminaHumanv4). R package version 1.26.0. *illuminaHumanv4.db* https://doi.org/10.18129/B9.bioc.illuminaHumanv4.db (2015).
79. Therneau, T. M., Crowson, Cynthia S., Atkinson, Elizabeth J. A Package for Survival Analysis in R. R package version 3.5-5. *The Comprehensive R Archive Network* (2023).

Acknowledgements

We thank Diana Lim and Nikita Abraham for preparation of scientific graphics and illustrations; J.P. Snook for technical support; the Cell Response and Regulation (CRR) Program from the Huntsman Cancer Institute (HCI); HCI Shared Resources: Research Histology, Research Immunohistochemistry, High Throughput Genomics and Cancer Bioinformatics, Cancer Biostatistics and Preclinical Research Resource; University of Utah Flow Cytometry Core and the Genomics Core; MD Anderson Cancer Center Functional Proteomics Core; the Leeds Institute of Cancer and Pathology, University of Leeds, U.K.; Qi Liu, Hua-Chang Chen and Jing Yang (Vanderbilt University Medical Center) for Cancer-Immu technical support; the Health Data Analytics and Statistics Center, Office of Data Science, Taipei Medical University for statistical support. This project was supported by funding from NIH/NCI P30CA042014 (HCI). A.H.G. has been supported by the American Cancer Society 133649-RSG-19-019-01-CSM and NIH/NCI K08CA188563 and is currently supported by the Department of Pathology at the University of Utah, NIH/NCI R37CA230630 and U.S. Department of Defense (DoD) W81XWH2210910. S.L.H. is supported by NIH/NCI R01CA121118. M.A.W. is supported by DoD W81XWH2210776. K.C.F. is supported by NIH R01AI158710. M.A.D. is supported by the Dr. Miriam and Sheldon G. Adelson Medical Research Foundation, the AIM at Melanoma Foundation, the NIH/NCI P50CA221703, the American Cancer Society, the Melanoma Research Alliance, Cancer Fighters of Houston, the Anne and John Mendelsohn Chair for Cancer Research, and philanthropic contributions to the Melanoma Moon Shots Program of MD Anderson.

Author contributions

Conceptualization, A.H.G, Y.W.; investigation, Y.W., J.W., E.C.W, C.P.R., A.R., E.D., J.K.H.T., R.K.W., A.H.G.; formal analysis, C.S., K.B. J.M.O, K.C.F., H.A.E.; methodology, S.L.H., K.C.F, M.A.W., A.H.G.; resources, Z.T., M.A.W., S.L.H., Y.N.V.G., M.A.D.; supervision, A.H.G., R.K.W., K.C.F., M.A.W., S.L.H.; writing-original draft, A.H.G, Y.W.; writing-reviewing & editing, A.H.G, Y.W., J.W., E.C.W., J.K.H.T., R.K.W.; funding acquisition, A.H.G.

Competing interests

M.A.D. has been a consultant to Roche/Genentech, Array, Pfizer, Novartis, BMS, GSK, Sanofi-Aventis, Vaccinex, Apexigen, Eisai, Iovance, Merck, and ABM Therapeutics, and he has been the PI of research grants to MD Anderson by Roche/Genentech, GSK, Sanofi-Aventis, Merck, Myriad, Oncothyreon, Pfizer, ABM Therapeutics, and LEAD Pharma. The remaining authors declare no competing interests.

Additional information

Supplementary information The online version contains supplementary material available at https://doi.org/10.1038/s41467-024-50881-1.

Correspondence and requests for materials should be addressed to Allie H. Grossmann.

Peer review information *Nature Communications* thanks Hisataka Sabe and the other, anonymous, reviewer(s) for their contribution to the peer review of this work. A peer review file is available.

[1]Department of Pathology, University of Utah, Salt Lake City, UT, USA. [2]Huntsman Cancer Institute, Salt Lake City, UT, USA. [3]Department of Oncologic Sciences, University of Utah, Salt Lake City, UT, USA. [4]Department of Melanoma Medical Oncology, The University of Texas MD Anderson Cancer Center, Houston, TX, USA. [5]Department of Molecular Biology and Genetics, Izmir Institute of Technology, Gulbahce, Urla, Izmir, Turkey. [6]Bioinformatics Shared Resource, Huntsman Cancer Institute, Salt Lake City, UT, USA. [7]Cancer Biostatistics Shared Resource, Huntsman Cancer Institute, Salt Lake City, UT, USA. [8]Department of Surgery, University of Utah, Salt Lake City, UT, USA. [9]Present address: School of Dentistry, Taipei Medical University, Taipei, Taiwan. [10]Present address: Providence Cancer Institute of Oregon, Earle A. Chiles Research Institute, Portland, OR, USA. [11]These authors contributed equally: Yinshen Wee, Junhua Wang. ✉e-mail: allie.grossmann@providence.org